

Toward High-Efficiency Photovoltaics-Assisted Electrochemical and Photoelectrochemical CO₂ Reduction: Strategy and Challenge

Jin Hyuk Cho¹, Joonhee Ma², and Soo Young Kim²

¹Affiliation not available

²Korea University

January 12, 2023

Abstract

The realization of a complete techno-economy through a significant carbon dioxide (CO₂) reduction in the atmosphere has been explored in various ways. CO₂ reduction reactions (CO₂RRs) can be induced using sustainable energy, including electric and solar energy, using systems such as electrochemical (EC) CO₂RR and photoelectrochemical (PEC) systems. This study summarizes various fabrication strategies for non-noble metal, copper-based, and metal-organic framework-based catalysts with excellent FE for target carbon compounds, and for noble metals with low overvoltages. Even though EC and PEC systems exhibit high energy-conversion efficiency using excellent catalysts, they are not completely bias-free operations because they require external power. Therefore, photovoltaics, which can overcome the limitations of these systems, have been introduced. The utilization of silicon and perovskite solar cells for photovoltaics-assisted EC (PV-EC) and photovoltaics-assisted PEC (PV-PEC) CO₂RR systems are cost efficient, and the III-V semiconductor photoabsorbers achieved high solar-to-carbon efficiency. This review focuses on all the members composed of PV-EC and PV-PEC CO₂RR systems and then summarizes the special cell configurations, including the tandem and stacked structures. Moreover, current problems such as a low energy conversion rate, expensive PV, theoretical limitations, and scale-up to industrialization are discussed with the suggested direction.

Title

Toward High-Efficiency Photovoltaics-Assisted Electrochemical and Photoelectrochemical CO₂ Reduction: Strategy and Challenge

Jin Hyuk Cho¹, Joonhee Ma¹, Soo Young Kim¹

¹Department of Materials Science and Engineering, Korea University, Seoul, Republic of Korea

Correspondence

Soo Young Kim, Department of Materials Science and Engineering, Korea University, Seoul 02841, Republic of Korea

Email: sooyoungkim@korea.ac.kr

Jin Hyuk Cho, Joonhee Ma contributed equally to this work.

Funding information

National Research Foundation of Korea, Grant/Award Numbers: 2021R1A4A3027878, 2022M3H4A1A01012712

Abstract

The realization of a complete techno-economy through a significant carbon dioxide (CO_2) reduction in the atmosphere has been explored in various ways. CO_2 reduction reactions (CO_2RRs) can be induced using sustainable energy, including electric and solar energy, using systems such as electrochemical (EC) CO_2RR and photoelectrochemical (PEC) systems. This study summarizes various fabrication strategies for non-noble metal, copper-based, and metal-organic framework-based catalysts with excellent FE for target carbon compounds, and for noble metals with low overvoltages. Even though EC and PEC systems exhibit high energy-conversion efficiency using excellent catalysts, they are not completely bias-free operations because they require external power. Therefore, photovoltaics, which can overcome the limitations of these systems, have been introduced. The utilization of silicon and perovskite solar cells for photovoltaics-assisted EC (PV-EC) and photovoltaics-assisted PEC (PV-PEC) CO_2RR systems are cost efficient, and the III-V semiconductor photoabsorbers achieved high solar-to-carbon efficiency. This review focuses on all the members composed of PV-EC and PV-PEC CO_2RR systems and then summarizes the special cell configurations, including the tandem and stacked structures. Moreover, current problems such as a low energy conversion rate, expensive PV, theoretical limitations, and scale-up to industrialization are discussed with the suggested direction.

KEYWORDS

Catalysts, electrochemical CO_2 reduction reaction, photoelectrochemical CO_2 reduction reaction, photovoltaic cell

1 INTRODUCTION

Since the 19th century, the acceleration of industrial development has led to the enormous combustion of fossil fuels.^[1] The excessive emission of carbon dioxide (CO_2) generated during the burning of fossil fuels accumulates in the atmosphere and traps greenhouse gases that cause not only abnormal climates such as cyclones, floods, and droughts, but also anthropological problems.^[2-3] Therefore, there is an urgent need to find a variety of sustainable and renewable energy sources to replace fossil fuels.^[4,5] Currently, to deal with this problem, electrochemical (EC) and photoelectrochemical (PEC) reactions with the CO_2 reduction reaction (CO_2RR) are considered as efficient potential solutions owing to their high energy efficiency and low cost.^[6-8] CO_2RR not only reduces the concentration of CO_2 in the atmosphere but also produces additional value-added carbon compounds.^[4,9] However, CO_2 molecules are extremely inert gases in the atmosphere owing to the thermochemically stable activity of the C=O bond; therefore, it is imperative to utilize efficient catalysts.^[10,11] Moreover, photovoltaics (PV), using sustainable solar energy, is capable of serving additional power to the CO_2RR system in combination with EC and PEC systems, which are known as photovoltaic-electrochemical (PV-EC) and photovoltaic-photoelectrochemical (PV-PEC) systems, respectively.^[12] These systems require 2.6 V to carry out the oxygen evolution reaction (OER) at the anode and CO_2RR at the cathode, which can be supplied by a solar cell.^[13] Therefore, designing efficient OER and CO_2RR catalysts, as well as innovative PV device systems, is essential for achieving high solar-to-carbon (STC) energy conversion efficiency.^[14,15] As depicted in Scheme 1, we organized advances in the PV-assisted CO_2RR for techno-economy.

In this review, the current challenges of PV-EC and PV-PEC cell systems, such as theoretical limitations due to the inherent semiconductor bandgap, inhomogeneous uniformity owing to increased active area, and efficiency degradation, are discussed. In particular, we focus on EC and PEC catalysts because carbon compounds are manipulated during CO_2RR through sequential electron and charge transfer,^[16] determined by the free Gibbs energy of CO_2 absorption and the desorption energy of the products between the interface of the CO_2 molecules and the catalyst electrode.^[15,17,18] Although noble metals are not competitive in terms of industry, gold (Au) and silver (Ag) have many advantages, including low overpotential and high Faradaic efficiency (FE) over a wide range of potentials for the formation of CO from CO_2 ,^[19-21] thus, noble metals can serve as cathode parts of PV-EC and PV-PEC because of their advantages. Furthermore, non-noble, metal-organic framework (MOFs)-based, and single-atom-based catalysts as state-of-the-art catalysts^[22-24] have been described owing to their abundant reserves, unique morphology, reconstruction, superior electron-charge transfer, excellent utilization, and tunable band gap energy.^[25] In addition, only copper (Cu) is

feasible among the diverse elements to produce C₂₊ carbon compounds via continuous C-C coupling under CO₂RR. [26,27] Therefore, we briefly explain intensive efforts to attain high selectivity for the desired carbon compounds by manipulating the surface facets of Cu, restructuring the morphology of Cu nanostructures, and causing synergistic effects from heterogeneous catalysts. [28-30] To accomplish a complete techno-economy, PV provides new possibilities to convert STC efficiency with minimal energy consumption by constructing self-contained PV-integrated CO₂RR reactors. [31] Therefore, the performance of the PV-EC and PV-PEC type of CO₂RR system that combines various types of PV including Si-based, [32] perovskite-based, [33] and GaAs-based [34] as well as tandem structures is introduced by analyzing the current/current density– voltage ($I/J-V$) characteristics. [35]

2 ELECTROCHEMICAL CO₂RR

Among all the CO₂ conversion methods, the electrochemical reduction of CO₂ is particularly attractive because of its advantages, such as an easy operating system and controllable process. [36-37] Currently, various types of electrocatalysts such as metals, [38-39] metals oxides, [40] alloys, [41] and single-atom catalysts, [42-44] have been studied to improve the performance of the CO₂RR. Electrocatalysts are divided into four groups: noble metals, non-noble metals, copper (Cu)-based, and single-atom catalysts (SAC).

2.1 Noble metal

Noble metal-based electrocatalysts (Au, Ag, and Pd) usually show efficient catalytic activity and selectivity, especially in CO₂ to CO conversion. Hsieh et al. fabricated Ag nanocoral catalysts via an oxidation-reduction process using chloride anions to promote the intrinsic electrocatalytic activity of bulk Ag. [45] As a result, the Ag nanocoral catalyst demonstrated a high CO₂RR performance with FE for CO (FE_{CO}) of 95 % at a low overpotential of 0.37 V vs. reversible hydrogen electrode (RHE), and high long-term stability for 72 h at -0.6 V vs. RHE. These results indicate that the presence of chloride anions plays a significant role in the enhancement of CO₂ reduction performance. Vertically standing Ag nanowire arrays (NWAs) with outstanding electrocatalytic performance have been reported using an easy nanomolding method (Figure 1(A)). [46] This facile method increases the electrical conductivity of electrocatalysts and facilitates the charge transfer process, leading to a more efficient CO₂RR. Two different types of anode aluminum oxide (AAO) templates were used to fabricate Ag-200 nm and Ag-30 nm NWAs. As shown in Figure 1(B), the as-synthesized Ag-200 nm NWA exhibited nanoarray morphologies. As compared to Ag-30 nm NWAs, Ag-200 nm NWAs showed excellent activity and selectivity toward CO with a lower onset potential of ~200mV, maximum FE_{CO} of 91 % at -0.6 V vs. RHE, and current density for CO (j_{CO}) of up to 4.47 mA cm⁻² (Figure 1(C) and (D)).

Zhu et al. fabricated ultrathin Au nanowires (NWs) using seed-mediated growth method for reducing CO₂ to CO. [47] Electrochemical measurements indicated that the Au NWs demonstrated high activity and selectivity toward CO with an onset potential of -0.2 V vs. RHE, FE up to 94 % at -0.35 V vs. RHE, and great stability of 6 h at -0.35 V vs. RHE in the CO₂-saturated 0.5 M KHCO₃. Chen et al. demonstrated facile EC alloying/dealloying of polycrystalline Au with a mixture of ethylene glycol and ZnCl₂ for the fabrication of three-dimensional (3D) nanoporous Au electrocatalysts (Figure 1(E)). [48] Further acid treatment with H₂SO₄ followed by calcination at 150°C, resulted in enhanced catalytic performance due to the creation of new active sites. The EC measurements indicate that the nanoporous Au exhibited excellent electrocatalyst performance toward CO with a maximum FE of 95.86 % at the applied potential of -0.6 V vs. RHE in a CO₂-saturated 0.1 M NaHCO₃ solution (Figure 1(F)). Shao et al. proposed twisted Pd–Au NWs with a unique core–shell using a simple template-free approach. [49] The optimized Pd–Au NWs displayed outstanding performance compared with Pd nanoparticles with a maximum CO FE of 94.3 % at -0.6 V vs. RHE, and a low overpotential of 90 mV.

2.2 Non-noble metal

Among non-noble metals, transition metals such as Ni, Zn, and Fe are the most popular.

Luo et al. electrodeposited Zn²⁺ on Cu mesh to fabricate highly porous Zn catalysts. [50] scanning electron mi-

croscopy (SEM) images of the electrodeposited Zn catalysts revealed that the corresponding electrocatalysts had highly porous structures, resulting in superior performance (Figure 1(G)). Specifically, Zn electrocatalysts exhibit FE_{CO} of 95 % and a current density of 27 mA cm^{-2} at -0.95 V vs. RHE in H-type cell, (Figure 1(G)) and 84 % FE_{CO} and current density of 200 mA cm^{-2} in a flow cell (Figure 1(I)). These outstanding performances are attributed to the highly porous structure of P-Zn, which increases the active site density and enhances the local pH effect, further surpassing the hydrogen evolution reaction (HER). Jiang et al. synthesized surface-regulated Ni nanoparticles supported on N-doped CMK-3 via pyrolysis of Ni^{2+} and Zn^{2+} pre-absorbed CMK-3 and urea in argon.^[51] By coordinating with N and O, the as-synthesized electrocatalyst exhibits electronic properties different from metallic Ni, resulting in an exceptional CO FE of 97 %, a high CO partial current density of 13.01 mA cm^{-2} , and a turnover frequency of 4.25 s^{-1} . Li et al. demonstrated a PCN-222(Fe)/CNTs catalyst by loading PCN-222(Fe) onto CNTs through an in situ solvothermal synthesis process, resulting in an unprecedented high activity and selectivity for CO_2 reduction.^[52] Due to the synergistic effect between PCN-222(Fe) and CNTs, the electrocatalyst exhibited exceptional electrocatalytic performance with a FE_{CO} of 95.5 %, TOF of 448.76 h^{-1} , and high durability over 10 h at -0.6 V vs. RHE .

Metal-organic frameworks (MOF) are promising nanomaterials for the CO_2 RR because of their large specific surface area, adjustable porosity, and composition.^[53-54] Kang et al. used zeolitic imidazolate frameworks (ZIFs), which are a subclass of MOFs, as electrocatalysts for the reduction of CO_2 to CO.^[55] Three different ZIF-8 catalysts were synthesized using various Zn sources: $ZnSO_4$, $Zn(NO_3)_2$, and $Zn(AC)_2$. EC measurements demonstrated that ZIF-8 prepared with $ZnSO_4$, showed excellent CO selectivity under a wide potential range from -1.5 to -1.9 (V vs. SCE) , reaching a maximum FE of 65.5 % at -1.8 (V vs. SCE) . Similarly, ultrasmall ZIF-8s were fabricated using a facile sol-gel method by Wang et al., and SEM images revealed that the as-synthesized ZIF-8 exhibited an orthododecahedral structure with a size of 80 nm. Ultrasmall ZIF-8 electrocatalysts display FE_{CO} of 90 % at -1.5 V vs. RHE with a partial current density of $\sim 5 \text{ mA cm}^{-2}$ and long-term stability of 12.5 h at -1.8 (V vs. RHE) .^[56]

Various metals, including Bi, Sn, and Cu, are considered efficient electrocatalysts for the conversion of CO_2 to formate ($HCOO^-$). Among them, Bi has attracted much attention in CO_2 RR owing to its large HER overpotential and the strong binding energy of $*OCHO$ species. For example, Zhang et al. fabricated a high-performance Bi-Zn bimetallic catalyst by surface modification of a Zn catalyst through a hydrothermal procedure with different concentrations of $Bi(NO_3)_3$ solution.^[57] The optimized Bi-Zn bimetallic catalyst showed maximum formate FE of 94 %, a current density of 3.8 mA cm^{-2} , and long-term stability of 7 h under -0.8 V vs. RHE with CO production of less than 10 % over the entire potential area (Figure 2(A) and (B)). Bifunctional interfaces between the bimetal and grain boundaries were attributed to the superb selectivity toward formate by favoring $*OCHO$ intermediate adsorption on the catalyst surface (Figure 2(C)). Lee et al. demonstrated a novel approach for the construction of Bi nanoflakes using the pulse-electrodeposition method for the conversion of CO_2 to formate.^[58] Various Bi nanostructures have been obtained using different electrodeposition methods. As shown in Figure 2(D), nanodot-shaped Bi particles and dendrite-shaped Bi were obtained using DC-60s and DC-120s, respectively, and Bi nanoflakes were synthesized using pulse deposition for six cycles (PC-6c). The Bi nanoflakes electrocatalysts exhibited exceptional CO_2 RR performance with formate FE of 79.5 % at -0.4 V vs. RHE and achieved a maximum FE up to $\sim 100 \%$ at -0.6 V vs. RHE (Figure 2(E)). Moreover, Bi nanoflakes showed excellent long-term durability of 10 h at -0.8 V vs. RHE without significant decay of FE_{CO} . Recently, nanoporous bismuth (np-Bi) with a 3D ligament-channel network structure was synthesized using a chemical dealloying approach.^[59] $Mg_{92}Bi_8$ consisting of Mg and Mg_3Bi_2 was selected as the precursor, and Mg completely dissolved in tartaric acid, while Bi maintained stability during the process. Consequently, np-Bi exhibited an outstanding formate FE of 94 % at -0.9 V vs. RHE with a maximum partial current density of 62 mA cm^{-2} -1.2 V vs. RHE in an H-cell and remarkable current density of 500 mA cm^{-2} at a low overpotential of 420 mV in a flow cell.

2.3 Copper based

Copper is one of the few metals that can efficiently convert CO_2 to hydrocarbons such as methane (CH_4) and ethylene (C_2H_4), owing to the moderate adsorption energy of the $*CO$ intermediate.^[38,60-61] Because the

electrocatalytic performance of Cu electrodes is usually determined by the Cu crystal facets, shape control of Cu nanoparticles (NPs) has been widely studied for desirable CO₂RR selectivity.^[62] Zhang et al. synthesized nanodeficient Cu nanosheets using an electrochemical reduction method.^[63] Cu nanosheet electrocatalysts with defects exhibited a better total current density, maximum ethylene FE of 83.2 % at -1.18 V vs. RHE without CO generation, and partial current density of up to 66.5 mA cm⁻² at -1.48 V vs. RHE, which is much higher than those of its counterparts (Figure 2(F)–(H)). Such nanodeficient structures promote ethylene production by enhancing the adsorption of intermediates and hydroxyl ions on the electrocatalyst.

Recently, simple approaches have been reported for fabricating ultrathin CuO nanoplate arrays through anodic oxidation for the conversion of CO₂ to C₂H₄.^[64] Benefitting from stable Cu/Cu₂O interfaces, the catalyst exhibits remarkable C₂H₄ FE of 84.5 %, partial current densities of 92.5 mA cm⁻² at -0.81 V vs. RHE, and high stability for 55 h. Yang et al. prepared one-dimensional ultrathin 5-fold twinned copper NWs for conversion of CO₂ to methane.^[65] Corresponding SEM and transmission electron microscopy (TEM) images revealed ultrathin NW structures with diameters of ~20 nm. Owing to its abundant edge sites, Cu NWs showed outstanding CH₄ selectivity with a maximum FE_{CH₄} up to 55 % at -1.25 V vs. RHE and selectivity.

2.4 Single atom catalyst

Single-atom catalysts (SACs) feature isolated metal atoms anchored on a support material as active sites.^[53,66] Compared to traditional catalysts, such as nanoparticles/clusters, SACs maximize the efficiency of metal atom utilization by nearly 100 %, resulting in a larger exposure of active sites, which leads to outstanding catalytic activity, excellent product selectivity, and stability.^[66-69] Among the various types of metals, Ni-, Fe-, and Co-based SACs have been proven to exhibit outstanding CO₂RR performance. Li et al. synthesized Ni SACs with Ni-N₄ active sites using a topochemical transformation method for converting CO₂ to CO.^[70] This strategy prevents Ni atoms from agglomerating, providing abundant active sites and consequently improving the CO₂RR performance. The as-prepared electrocatalyst demonstrates remarkable FE_{CO} over 90 % in a wide potential range from -0.5 to -0.9 V vs. RHE and reached a maximum FE_{CO} up to 99 % at -0.81 V vs. RHE with a current density of 28.6 mA cm⁻². Yan et al. fabricated coordinatively unsaturated Ni-N active sites anchored on porous carbon by high-temperature calcination of Zn/Ni bimetallic ZIF-8.^[71] As prepared Ni SACs electrocatalyst showed high FE_{CO} of 92.0–98.0 % over a wide potential window of -0.53 to -1.03 V vs. RHE, current density of up to 71.5 ± 2.9 mA cm⁻², and exceptional TOF of 10,087 ± 216 h⁻¹ at -1.03 V vs. RHE. Density functional theory (DFT) calculations indicated that such a coordinatively unsaturated Ni-N site contributed to enhancing the CO₂RR performance, outperforming the HER. Pan et al. fabricated an efficient CO₂RR electrocatalyst with Co sites atomically dispersed on polymer-derived hollow N-doped porous carbon spheres (HNPCs) (Figure 3A).^[72] Field-emission scanning electron microscopy (FE-SEM) and high-resolution TEM images of the HNPCs indicated a uniform hollow spherical structure. Owing to their large surface area, abundant active sites, and high electrical conductivity, HNPCs demonstrated high CO₂RR performance toward CO with FE above 90 % under a wide potential range from -0.57 to -0.88 V vs. RHE and reached maximum FE of 99.4 % at -0.79 V vs. RHE (Figure 3B). Xin et al. synthesized Zn SAs anchored onto microporous N-doped carbon (SA-Zn/MNC) using dissolution and carbonization methods for the CO₂RR to CH₄.^[73] Owing to its conductivity and highly exposed active sites, as-prepared SA-Zn/MNC showed FE_{CH₄} of 85 % at -1.8 (V vs. SCE), the partial current density of -31.8 mA cm⁻², and outstanding long-term stability for 35 h. Recently, Wu et al. produced atomically dispersed Fe atoms coordinated to N (Fe-N) within carbon nanorods (Fe-N-C) through high-temperature pyrolysis of a 3D sea urchin-like FeOOH-polyaniline (FeOOH-PANI) composite.^[74] Owing to its highly porous structure with abundant exposed active sites, as well as its large specific surface area, the optimized Fe-N-C electrocatalyst exhibited a high FE_{CO} of 95 % at a small overpotential of 530 mV with j_{CO} of 1.9 mA cm⁻². Guao et al. fabricated Sn SACs with atomically dispersed SnN₃O₁ active sites embedded in an N-rich carbon matrix for an efficient EC conversion of CO₂ to CO.^[75] Unlike the Sn-N₄ configuration, asymmetric SnN₃O₁ configurations show superior performance for the conversion of CO₂ to CO with a maximum FE of 94 %, CO partial current density of 13.9 mA cm⁻² at -0.7 V vs. RHE, and extraordinary TOF of 23,340.5 h⁻¹ (Figure 3C,D). DFT calculations demonstrated that the unique SnN₃O₁ configuration of the Sn SACs electrocata-

lysts decreased the activation energies required to form *CO and *COOH , further facilitating CO formation (Figure 3E). To develop high-performance SACs electrocatalysts, heteroatoms such as S,^[76-77] B,^[78] and P^[79] were introduced to alter the coordination environment of the center atoms and electronic structures.^[80] Liu et al. developed a B/N co-doped carbon matrix anchored with single atomic Fe sites (Fe-SA/BNC) using ferroceneboronic acid (FBA) for doping Fe and B into ZIF-8 with a one-to-one atomic ratio of Fe and B.^[81] FBA@ZIF-8 was first synthesized and Fe-SA/BNC was subsequently obtained via high-temperature calcination at 900degC for 2 h. The Fe-SA/BNC exhibited outstanding CO₂RR performance with a FE_{CO} up to 94 % at -0.7 V vs. RHE, a current density of ~ 25 mA cm⁻², and remarkable long-term stability of 30 h using H-cell and FE_{CO} of 99 %, current density of 130 mA cm⁻² using membrane electrode assembly (MEA) (Figure 3(F)–(H)). These electrochemical test results emphasize the importance of introducing boron into Fe-SA/NC. The diverse electrocatalysts used for the CO₂RR are summarized in Table 1.

3. PHOTOELECTROCATALYTIC CO₂ REDUCTION

Photoelectrochemical (PEC) CO₂ reduction possesses the advantages of both photocatalytic and electrocatalytic CO₂ reduction and has attracted a great deal of interest.^[82-84]

PEC CO₂RR proceeds through the following steps:^[83]

- (1) Generation of electron-hole pairs.
- (2) Charge separation/transport by an external bias.
- (3) Surface redox reactions:

A large amount of electron-hole recombination occurs at each stage, releasing energy as light or heat. Therefore, the separation and transfer of photogenerated carriers in semiconductors are key factors for effectively improving the solar conversion efficiency.

Enormous efforts have been devoted to the design and engineering of photocathodes, such as doping,^[85-86] nanostructuring,^[87-89] and co-catalyst loading^[84]. Among these, coupling a co-catalyst with a light-absorbing semiconductor is one of the most effective approaches for improving PEC performance. Normally, bare semiconductor surfaces are inert and can barely activate CO₂ molecules, leading to poor PEC CO₂RR performance. To solve these problems, various types of co-catalysts have been loaded on the photoelectrode to reduce the activation energy for CO₂ reduction and suppress surface charge recombination, thus accelerating the surface reaction kinetics.

3.1 Noble metal

Noble metals, including Au, Ag, Pt, Pd, Ru, and Rh, are known to be the most active co-catalyst for PEC CO₂ reduction owing to their high catalytic activity and selectivity. Song et al. demonstrated a nanoporous mesh-type Au thin-film co-catalyst loaded onto a Si photocathode via mild electrochemical oxidation and reduction of the Au thin film (Figure 4(A)).^[90] As shown in Figure 4(B), the current density and onset potentials of all RA-Au thin films were significantly improved compared with those of the untreated Au thin-film. The optimized co-catalyst showed outstanding performance toward PEC reaction for the reduction of CO₂ to CO with an FE of up to 91 % at the CO₂/CO equilibrium potential of -0.11 V vs. RHE in an aqueous solution under 1 sun illumination (Figure 4(C)). To design an efficient semiconductor/co-catalyst interface, Jang et al. prepared a ZnTe/ZnO photocathode with Au nanoparticles deposited using an e-beam evaporator.^[91] By loading Au NPs onto a photocathode, a Schottky junction was formed at the interface between the Au NPs and ZnTe, resulting in the improved separation of photogenerated carriers and electron transfer into the electrolyte. As a result, Au-coupled ZnTe/ZnO-NW photocathode delivered outstanding PEC performance with a photocurrent density of -16.0 mA cm⁻² and incident photon-to-current conversion efficiency of 97 % compared with those of a bare electrode (-7.9 mA cm⁻², 68 %). Recently, Wang et al. developed a novel strategy for producing highly efficient PEC photocathodes by coupling plasmonic Au NPs and n+p-Si through a TiO₂ interlayer.^[92] The Au/TiO₂/n+ p- Si photocathode produced 86 % FE_{CO} with a partial current density of -5.52 mA cm⁻² at -0.8 V vs. RHE (Figure 4(D) and (E)). DFT calculations indicated

that the synergistic effect of layering Au and TiO₂ facilitated *COOH formation and *CO desorption, thereby promoting the conversion of CO₂ to CO (Figure 4(F)). An innovative method of controlled chemical etching on Si wafers using etching solutions containing Ag⁺ ions was reported to synthesize a Si surface uniformly deposited with an Ag particulate film.^[93] The PEC performance of the method was excellent with a large photocurrent density of ~10 mA cm⁻² under 0.5 sun, outstanding FE of ~90 % at 0.5 V vs. RHE for CO, and excellent stability of 8 h.

3.2 Non-noble metal

Despite the prominent PEC CO₂RR of noble metal-based co-catalysts, their high cost and scarcity limit large-scale CO₂ conversion. Hence, the development of inexpensive catalysts with sufficiently high activity and stability is essential. Bi- and Sn-based co-catalysts are well known for their particularly high selectivity for the reduction of CO₂ to formate (HCOOH). Choi et al. prepared heterojunction Sn-coupled p-Si NWs using an Ag-catalyzed electroless chemical etching method.^[94] HR-TEM and HAADF-STEM measurements indicated the uniform distribution of Sn nanoparticles on the wire array. These heterojunction wire/Sn arrays show extraordinary PEC performance toward HCOOH, compared with planar p-Si and wire arrays with FE of 40 % and 88 % in single-cell and H-type cells, respectively. Recently, Ding et al. prepared Si/Bi photocathodes with an enhanced interface through the Bi³⁺-assisted chemical etching of Si wafers and assessed their PEC CO₂ reduction performance.^[95] The optimized Si/Bi photocathodes exhibit outstanding catalytic activity, with a positive onset potential, large photocurrent density of 10 mA cm⁻² under 0.5 sun, and high formate FE of up to 90 % (Figure 4(G)). Moreover, the photocurrent density was improved up to 12 mA cm⁻² when the Si surface was exposed using the photolithography method (Figure 4(H)). Ma et al. demonstrated core-shell-structured Ni@In co-catalyst loaded p-type Si nanowire arrays (SiNWs) for the reduction of CO₂ to formate.^[96] P-type SiNWs were synthesized via a metal-assisted chemical etching method, and Ni@In/SiNWs photocathodes were subsequently fabricated by a photodeposition approach. As a result, compared with pristine SiNWs, Ni@In/SiNWs catalyst showed better performance for CO₂ to HCOOH conversion with a formation rate of 58 μmol h⁻¹ cm⁻² as well as high FE, 87 % at -1.2 V vs. RHE.

3.3 Copper based

Deng et al. synthesized a Cu₂O photocathode coated with a metal-organic framework (MOF) material, Cu₃(BTC)₂, which could protect the underlying Cu₂O from undesirable photocorrosion, facilitate charge separation and electron transfer to active sites, and provide abundant active sites for catalytic CO₂ reduction.^[97] The obtained Cu₃(BTC)₂/Cu₂O photocathode with abundant active sites exhibited a maximum CO selectivity of up to 95 % and STC efficiency of 0.83 % at -2.07 (V vs. Fc/Fc+), surpassing those of a bare Cu₂O electrode. Zhao et al. reported a Cu-decorated Co₃O₄ nanotube electrode for PEC CO₂ reduction to formate.^[98] Co₃O₄NTs were first constructed on Co foil by anodization, and Cu electrodeposition was subsequently performed to synthesize metallic Cu-loaded Co₃O₄ nanotube array electrodes. Because Cu NPs are positively charged due to their interaction with Co₃O₄, CO₂ adsorption on Cu NPs occurs in the form of O-Cu, promoting the protonation of the carbon atom, resulting in the formation of formate. This synergistic effect between Co₃O₄ NTs and metallic Cu NPs results in remarkable PEC CO₂ reduction performance with nearly 100 % selectivity and a maximum production rate of 6.75 mmol·L⁻¹·cm⁻² in 8 h PEC process, which is superior to Co₃O₄ NTs without metallic Cu NPs (Figure 4(I) and (J)). Table 2 summarizes the PEC-CO₂RR performance of the co-catalysts.

4 PHTOVOLTAIC-POWERED ELECTROCATALYTIC CO₂RR REACTOR

4.1 C₁ product

In most cathode electrodes of the PV-EC CO₂RR combination, CO₂RR and HER are dominant^[99-100] while the oxygen evolution reaction is dominant at the anode electrode.^[99] As described above, noble metal catalysts, including Au and Ag, with low overpotentials capable of suppressing hydrogen formation as well as active CO formation from CO₂ have been utilized as electrocatalyst cathodes. The CO₂RR characteristics of the catalyst were confirmed by FE, current density, and overpotential measurements.^[71,100]

Disordered Ag nanoparticles were used as the cathode to improve the selectivity and durability for CO₂ to CO formation, Pt foil was employed as the anode, and electrical energy was provided by a six-section a-Si PV cell. The SEM images show that the disordered Ag nanoparticles have an irregular size distribution, while the 3, 5, and 11 nm Ag on the carbon support are uniform in size.^[101] To confirm the FE_{CO} and j_{CO}, the CO₂RR performance of Ag nanoparticles was evaluated in an H-cell filled with a 0.1 M KHCO₃ electrolyte. While a maximum FE_{CO} of 83%, 90%, and 95% were confirmed on 3, 5, and 11 nm of Ag nanoparticles, respectively, disordered Ag exhibited FE_{CO} of more than 90% over a wide range of potentials -0.6 to -1.7 V vs. RHE (Figure 5A). In addition, the disordered Ag nanoparticles had j_{CO} of -16.7 mA cm⁻² higher than other uniform Ag nanoparticles at -1.8 V vs. RHE (Figure 5B). In addition, linear sweep voltage (LSV) measurements on disordered Ag were performed on CO₂RR at the cathode and OER at the anode to determine the required light-inducing voltage for driving the PV-EC system. The results indicated that a voltage of 2.4 V was required (Figure 5(C)). Six-section a-silicon-PV, which has an area of 25 cm² providing 3.38 V of a circuit voltage, was combined with the EC system to confirm the electrocatalytic performance of PV-EC (Figure 5(D)). As shown in Figure 5(E), during the PV-EC system test, a potential of 0.75 V was observed at the cathode electrode. Owing to the active proton-electron coupling transfer (PECT) process on disordered Ag, the selectivity of PV-EC performance exhibited a FE_{CO} of 92.7%, which is significantly higher than other uniform Ag catalysts (Figure 5(F)). Thus, owing to the excellent electrocatalytic properties with an appropriate Tafel slope (128 mV dec⁻¹) and overpotential, disordered Ag noble metals show high STC efficiency when combined with a-Si-PV.^[102-103] Another promising CO₂RR catalyst, which has high efficiency in CO formation when combined with a PV system, is Au, which is a noble metal. For example, Wang et al. fabricated needle-like nano-Au on carbon paper using a one-step electrodeposition method as a cathode for efficient CO₂RR and nanosheet-like NiFe hydroxide on Ni foam via a hydrothermal method as an anode for oxygen evolution.^[104] Needle-like nano-Au exhibited excellent electrochemical CO₂RR performance through low onset overpotential of less than 160 mV, a low Tafel slope of 47 mV dec⁻¹, and a maximum FE_{CO} of ~92% at -0.57 vs. RHE. To further explain the Tafel value, catalysts with low Tafel slopes indicate that the initial rate-determining chemical step is *COOH formation by facilitating the equilibrium state for the adsorbed CO₂⁻ intermediate. To build a complete PV-powered EC system efficiently, GaAs (InGaP/GaAs/Ge) was adopted, recoding a high photoconversion rate of 37.9% and stable durability of 24 h with an average FE_{CO} of 92% in a CO₂ saturated 0.5 M KHCO₃ electrolyte under continuous electrolysis. Lee et al. reported a carbon-supported tungsten-seed-based 3D silver dendrite (W@AgD) as a CO₂RR catalyst for CO formation, by investigating a zero-gap CO₂ electrolyzer.^[105] As shown in Figure 6(A) of the scheme of the STC system, in order to compose a complete PV-EC system, 3-6 silicon solar cells were assembled in series as modules with a size of 10 cm X 12 cm, and as the OER catalyst in charge of the anode part, Fe-doped Co foam, which exhibited high catalytic activity in alkaline media, was used. The assembled PV-EC system varied the number of silicon-based solar cells to confirm the optimized *I-V* curves and exhibited a high STC conversion rate of 12.1% with a current of 1.1 A under AM 1.5 G, which is close to the highest value among silicon-based PV-EC systems, and also exhibited excellent FE_{CO} of 95% (Figure 6(B) and (C)). Kim et al. reported another excellent PV-EC system that is advantageous for generating CO. Their system consisted of an Au₂₅ cluster placed on carbon paper and was used as a cathode, NiFe inverse opal was used as an anode, and Ga_{0.5}In_{0.5}P/GaAs tandem PV cell was the serving solar energy (Figure 6(D)).^[106] As displayed in Figure 6(E), the *I-V* characteristics of the individual series-connected Ga_{0.5}In_{0.5}P/GaAs tandem cell and CO₂ electrolyzer with Au₂₅ cluster, were confirmed to match interaction of two curves at -14 mA at 1.63 V. Moreover, the PV-EC system combined with the Au₂₅ cluster, NiFe inverse opal, and tandem solar cells exhibited an excellent average of solar to CO efficiency of 18% under continuous reaction for 12 h (Figure 6(F)). To attain a high STF efficiency, Chen et al. fabricated boron-doped bismuth (Bi(B)) by anticipating the unique electronic properties of Bi(B) that regulate the free energy of the OCHO* intermediate by inducing the movement of the p-electron state to the Fermi level.^[107] As shown in Figure 6(G), the STF efficiency was evaluated using Bi(B) as an efficient CO₂ catalyst and FeP nanosheets supported on Ni foam as an OER catalyst with commercial GaInP/GaInAs/Ge solar cells for efficient PV-EC devices. As a result, this PV-EC system achieved the best record of STC of 11.8%, accompanied by high FE for formate of 93% under the CO₂RR system (Figure 6(H) and (I)).

4.2 C₂₊ product

By coupling with PV, an EC system consisting of copper electrocatalysts is also utilized to efficiently reduce CO₂ for C₂₊ value-added hydrocarbons. Si (series) solar cells,^[108] dye-sensitized solar cell (DSSC) solar cells,^[109] copper-indium-gallium-selenide (CIGS) solar cells,^[110] and perovskite solar cells^[111] are some of the solar cell types that are used to provide insufficient energy to PV-integrated EC systems using copper-based electrocatalysts as a cathode.^[112] However, the conversion efficiency to C₂₊ using a copper still faces limitations compared to C₁ selectivity of over 90%. Therefore, to improve C₂₊ formation, various methods, including exposed facet,^[113-115] size effect,^[116] morphology change,^[117] defects,^[118] oxide state manipulation,^[119] and grain boundaries^[120] are explored from many perspectives. In addition, we discuss the ideal PV-EC in combination with an efficient copper catalyst fabricated by the above strategies. Chen et al. reported a grain-boundary-rich copper, which was fabricated by controlling the grain growth of copper via electrodeposition, as an efficient PV-EC CO₂RR electrocatalyst and achieved a high solar-to-C₂₊ conversion efficiency (STC).^[121] In electrochemical performance, grain-boundary-rich copper (GB-Cu) exhibited a remarkable FE of 73% for C₂₊ formation (propanol, ethylene, and ethanol) over a wide range of potentials, in particular, FE of 31.74% for ethanol was confirmed at a high current density of 45 mA cm⁻² at -1.3 V vs RHE. An assembled PV-EC system, which was composed of GB-Cu and Se-(NiCo)S_x/(OH)_x nanosheets as the cathode and anode, respectively, using six-series a-Si/c-Si heterojunction (SHJ) module as the photocathode, showed FE of 68% for C₂₊ formation and STC conversion efficiency of 3.88%, accompanied by well-matched LSV curves of each PV and EC system (Figure 7(A) and (B)). Huan et al. adopted an oxide-derived strategy for both cathode and anode catalysts, in which dendritic nanostructured copper oxide (DN-CuO) with efficient mass transfer by lowering mass transport losses was used to limit the poisoning of the cathode electrode.^[122] As illustrated in Figure 7(C) and (D), an electrochemical cell using DN-CuO as both electrodes exhibited low electrolyte resistance at a high current density (25 mA cm⁻²) at a cell potential below 3 V from the LSV curve and yielded a high production rate from FE toward C₂₊ formation. Zhang et al. achieved maximum FE of 58.6% for ethylene by fabricating Cu (100)-rich films reducing the energy barrier of C-C coupling formation using the dynamic deposition-etch-bombardment method and further applied the Cu (100)-rich films to the efficient cathode portion of the PV-EC system.^[123] As illustrated in Figure 7(E), a solar-driven electrochemical CO₂RR system was constructed, where high-power reactively sputtered Cu films (HRS-Cu) was used as the cathode and a Si photodiode was used as the solar energy absorber. From the *I-V* characteristic of the PV-EC device, the intersection of PV and electrocatalytic was confirmed at an operating current density of 2.41 V and current density of 41.3 mA under simulated AM 1.5G illumination, which displayed the maximum power point (MPP) matching of a solar panel, evaluating the solar-to-electricity conversion value of a PV-EC device (Figure 7(F)). As shown in Figure 7(G), total FE of ~72 % for C₂₊, ethylene of ~45%, and STC efficiency of ~6% with 40 mA of current were confirmed by chronoamperometry measurements under simulated AM 1.5G illumination for 220 min. In addition, to scale up the PV-EC system, a membrane electrode assembly system (MEA), which has advantages such as no requirement for additional catalyst loading steps, no electrode contamination, and suitability for large-area electrodes, was adopted (Figure 7(H)). When the cathode electrode was enlarged to 4cm² and 25cm², the current density and maximum FE for ethylene reached 120 mA cm⁻² and 58.6%, and 480 mA cm⁻² and 50.9%, respectively. Ideal PV-EC, which was reported by Cheng et.al, composed of selective electrodeposition of Cu catalysts on Ag catalyst prisms, covered with an optimal amount (35%) of surface area, exhibits excellent stability.^[124] As shown in Figure 7(I), a semitransparent metal prism array (PA) was connected to the top layer of triple junction (3 J) III-V semiconductors to suppress hydrogen evolution and achieve efficient light harvesting. The intersections between photovoltaics, including the Spectrolab stack, which is the light-limiting current in the middle cell, and FhG-ISE 3 J, which is the light-limiting current in the bottom cell, and electrocatalysts such as Ag-PA and Cu/Ag-PA with NiO_x as an anode, are displayed from *J-V* measurements in the 0.1 M CO₂-purged KHCO₃ (Figure 7(J) and (K)). Through the intersection of *J-V* curves between Ag-PA+NiO_x and Ag-PA-Spectrolab 3J, and Ag-PA-ISE 3J, cell voltage (U_{cell}) of 2.56 V and current (J) of 2.65 mA cm⁻² for Ag-PA-Spectrolab 3J and U_{cell} of 2.85 V and J of 5.13 mA cm⁻² for Ag-PA-ISE 3J are confirmed with high FE of ~80% for CO at broad cell voltages (2.5-2.9 V) (Figure 7(I) and (L)). When Cu was additionally electrodeposited on Ag-PA, the *J-V* intersection displayed a U_{cell} of 2.56 V and J of 2.60 for Spectrolab 3

J, and U_{cell} of 2.8 V and J of 5.97 mA cm⁻² for Ag-PA-ISE 3 J (Figure 7K). Cu/Ag-PA exhibited FE of approximately 30% for C₂H₅OH in the voltage range of 2.5–2.9 V as well as the formation of value-added C₂₊ carbon compounds (Figure 7(M)).

5. PHOTOVOLTAIC-POWERED PHOTOELECTROCATALYTIC CO₂RR REACTOR

The PV-EC system is operated by a sufficient driving force through solar energy from multi-junction PVs for CO₂RR. However, PV-PEC, which consists of a single-junction and multi-junction PV and a photoelectrode, absorbs light energy to generate voltage and current from the electrode and provides a redox reaction to the interfacing electrode.^[125]

As shown in Figure 8(A), Jang et al. designed the stacked tandem cell structure of a PV-PEC system for efficient STC conversion efficiency from a photoelectrode, which has excellent light harvesting of higher-energy photons, and from a single junction of perovskite PV, which has lower-energy photons.^[126] In a concrete structure, the gold-decorated triple-layer ZnO@ZnTe@CdTe (ZCT) core-shell nanorod array with facilitated charge separation and a narrow band gap with excellent catalytic efficiency was utilized as a photocathode, a CH₃NH₃PbI₃ perovskite solar cell in tandem was adopted for efficient light harvesting, and Co-Ci was situated in a light-blocked place as an OER anode. The absorption property, including incident photon-to-current conversion efficiency (IPCE), of two light absorbers under AM 1.5 G indicated that while the power density of Au nanoparticles decorated a ZCT (ZCT NR-Au) photocathode was reduced to 55%, accompanied by unchanged open-circuit voltage, most of light it used was below 550 nm, as shown in the Figure 8 (B) and (C). From the *J-V* characteristic, the operating point at the current of 0.85 mA was confirmed by the intersection of the perovskite solar cell and the photocathode in an unbiased tandem device for spontaneous photoelectrochemical CO₂RR (Figure 8(D)). Furthermore, the evolution of gaseous products containing CO and H₂ was measured for 3 h under 1 sun illumination by chronoamperometry with unbiased external voltage, and a ZnO@ZnTe@CdTe-Au photocathode with single-junction perovskite achieved FE of 74.9% for CO in the CO₂-purged KHCO₃, which shows excellent selectivity among induced corrosion of Te-based materials (Figure 8(E) and (F)). Similarly, the production of value-added products with tandem structures combined with solar cells and Cu-based photocathodes has attracted considerable attention. For the effective formation of HCOOH, one of the valuable C₁ products, Kim et al. introduced assembled FeOOH/BiO₄/CIGS tandem devices that do not require external bias such as 1.2 V.^[127] For the assembled tandem device, a single Cu(In,Ga)Se₂ (CIGS) solar absorber was utilized as a PV cell owing to its photo-advantages such as adequate direct band gap (1.12 eV) and excellent durability in an aqueous electrolyte under the CO₂RR system (Figure 8G). In addition, FeOOH/BiVO₄ adjusted in thickness, retained high stability and optimal current as a photoanode situated at the top cell, and a mesoporous indium tin oxide (*meso* ITO) cathode was used as the working electrode. As shown in Figure 8(H) and (I), photoelectrochemical profiles including *J-V* characteristics and chronoamperometry measurement of the combined CIGS-based tandem device compared to perovskite solar cell exhibited improved photoelectrochemical performance in the following metrics: an open-circuit voltage (0.64 V), short-circuit current density (35.68 mA cm⁻²), a fill factor (65%), and power conversion efficiency (15.01%). In contrast to the humidity-sensitive perovskite-based tandem cells showing formate formation below 5 Mm under relative humidity (RH) environments, FOOH/BiVO₄/CIGS/*meso* ITO CIGS-based system produced approximately 6 mM of formate concentration regardless of RH environment value of more than 80%. For efficient CO₂RR toward multi-carbon (C₂₊) formation by photovoltaic-biased photoelectrocatalysis, Gurudayal et al. designed a PV-PEC device utilizing an Ag-supported dendritic Cu as Si-photocathode (bottom photoabsorber), IrO₂ nanotube as an anode in tandem with two series-connected semi-transparent halide perovskite solar cell (top photoabsorber), which had a band gap of 1.58 eV under 1 sun illumination in 0.1 M CO₂-purged CsHCO₃ (Figure 8(J)).^[128] From the *J-V* curve of the photocathode and two series-connected PV intersections, operating currents of 2.1 to 2.9 mA depending on the concentrations of the CsHCO₃ electrolyte were confirmed (Figure 8(K)). The outstanding FE of the system for diverse carbon compounds by suppressing HER evolution and STC efficiency of 3.5% with unbiased external voltage are depicted in Figure 8(L). The use of perovskite solar cells, which are cost efficient, results in high STC efficiency by combining tandem devices with an efficient photocathode. The PV-EC and PV-PEC devices are listed in Table 3.

CONCLUSIONS AND PERSPECTIVE

In this review, we introduce diverse systems, including electrochemical (EC), photoelectrochemical (PEC), photovoltaic-assisted electrochemical (PV-EC), and photovoltaic-assisted photoelectrochemical (PV-PEC), for efficient CO₂ reduction and conversion to achieve carbon neutrality by introducing catalysts, photoabsorbers, and ideal bias-free PV-assisted devices. In the EC system, Cu, the only metal capable of producing high value-added C₂₊ carbon compounds, has limitations due to the lack of energy supply for the formation of C-C couplings, while electrocatalysts such as noble metals and MOF-based and single atom-based materials show excellent CO₂ conversion rates of approximately 100% for C₁ products. Therefore, as mentioned, designing Cu-based materials that establish various strategies, such as manipulating surfaces, reconfiguring morphology, and inducing synergies from heterogeneous catalysts, is imperative. Despite numerous efforts, the low FE toward C₂₊ chemicals is a problem to be solved from various perspectives, including not only the EC system but also PEC and PV-PEC devices. Moreover, obstacles to the PEC system, such as complex reaction paths, large photovoltage requirements, low solar-to-fuel efficiency, and poor light-harvesting properties, can be overcome by combining a co-catalyst with a light-absorbing semiconductor. Additionally, as in the EC system, manufacturing ideal PEC catalysts causing synergetic effects from heterogeneous materials and coating photocathodes with MOF materials may be a potential substitute for expensive noble metal catalysts, maintaining high energy conversion efficiency.

To acquire large-scale installations of CO₂RR devices, we proposed two novel PV-powered systems: PV-EC and PV-PEC. Both systems have an outstanding ability to lead the techno-economy to achieve high STC efficiency by serving the 2.6 V needed to reduce CO₂ from photovoltaics. However, large total voltage requirements, which are determined by analyzing intersections including the maximum power point (MPP) and operating point of current/current density – voltage ($I/J-V$) characteristics, remain a key hindrance. To overcome these challenges, Si-, perovskite-, DSSC-, CIGS-, and GaAs-based solar absorbers, as well as those of multi-junction or tandem structures, have gained a lot of attention. Nevertheless, Group III-V semiconductors composed of multi-component elements containing GaAs-based absorbers show excellent STC efficiency. However, they are not cost efficient for constructing light harvesting system. On the other hand, perovskite solar cells connected in series, which have tunable band gaps, high STC efficiency, high open-circuit voltages, and cost efficiency, exhibit a lack of long-term stability in the CO₂RR system. Therefore, for an ideal approach, the PV-PEC device, which operates by receiving a voltage from both the photocathode and the PV cell, not only requires a lower voltage than the PV-EC, but also generates a higher current density to ensure high STC efficiency. Overall, to realize bias-free PV-EC and PV-PEC devices, high-performance of various combinations of cathodes and anode catalysts, zero-gap electrolysis, and engineering series-connected photovoltaics are required, and further development is essential for industrial applications.

ACKNOWLEDGMENT

This research was supported by the NRF, funded by the Korean government [2021R1A4A3027878, 2022M3H4A1A01012712].

CONFLICT OF INTEREST

The authors declare no conflict of interest.

ORCID

Soo Young Kim <https://orcid.org/0000-0002-0685-7991>

REFERENCES

- [1] S. Chu, A. Majumdar, *Nature* **2012** ,488, 294–303.
- [2] S. E. Schwartz, *Energy Environ. Sci.* **2008** , 1, 430-453.
- [3] T. J. Crowley, R. A. Berner, *Science*, **2001** , 292, 5518.
- [4] Y. -H. Luo, B. -Z. Dong, J. Liu, S. -L. Li, Y. -Q. Lan, *Coord. Chem. Rev.* **2019** , 390, 86-126.

- [5] F. Pan, Y. Yang, *Energy Environ. Sci.* **2020** , 13, 2275-2309.
- [6] D. Johnson, Z. Qiao, A. Djire, *ACS Appl. Energy Mater.* **2021** , 4, 9, 8661–8684.
- [7] X. Wang, Y. Wang, X. Sang, W. Zheng, S. Zhang, L. Shuai, B. Yang, Z. Li, J. Chen, L. Lei, N. M. Adli, M. K. H. Leung, M. Qiu, G. Wu, Y. Hou, *Angew. Chem. Int. Ed.* **2021** , 60 , 4192.
- [8] S. Ji, Y. Qu, T. Wang, Y. Chen, G. Wang, X. Li, J. Dong, Q. Chen, W. Zhang, Z. Zhang, S. Liang, R. Yu, Y. Wang, D. Wang, Y. Li, *Angew. Chem. Int. Ed.* **2020** , 59 , 10651.
- [9] C. Kim, F. Dionigi, V. Beermann, X. Wang, T. Moller, P. Strasser, *Adv. Mater.* 2019, 31, 1805617.
- [10] M. C. O. Monteiro, M. F. Philips, K. J. P. Schouten, M. T. M. Koper, *Nat. Commun.* **2021** , 4943.
- [11] F. – Y. Gao, R. -C. Bao, M. -R. Gao, S. -H. Yu, *J. Mater. Chem. A* , **2020** ,8, 15458-15478.
- [12] T. N. Huan, D. A. D. Corte, S. Lamaison, D. Karapinar, L. Lutz, N. Menguy, M. Foldyna, S. -H. T. -Cruz, A. Hagfeldt, F. Vella, M. Fontecave, V. Mougel, *Proc. Natl. Acad. Sci. U.S.A.* **2019**, 116(20), 9735-9740.
- [13] Y. Zhang, C. Ye, J. Duan, H. Feng, D. Liu, Q. Li, *Front. Energy* **2022** , 10, 956444.
- [14] N. Kato, S. Mizuno, M. Shiozawa, N. Nojiri, Y. Kawai, K. Fukumoto, T. Morikawa, Y. Takeda, *Joule* , 2021, 5, 687–705.
- [15] C. E. Creissen, M. Fontecave, *Adv. Energy Mater.* **2021** , 11, 2002652.
- [16] K. Zhao, X. Nie, H. Wang, S. Chen, X. Quan, H. Yu, W. Choi, G. Zhang, B. Kim, J. G. Chen, *Nat. Commun.* **2020** , 11, 2455.
- [17] K. Xu, S. Ning, H. Chen, S. Ouyang, J. Wang, L. Song, J. Lv, J. Ye, *Sol. RRL* , **2020** , 4, 2000116.
- [18] T. Nishi, S. Sato, K. Sekizawa, T. M. Suzuki, K. Oh-ishi, N. Takahashi, Y. Matsuoka, T. Morikawa, *ChemNanoMat* **2021** , 7 , 596.
- [19] Y. Jiang, Y. Yu, X. Zhang, M. Weinert, X. Song, J. Ai, L. Han, H. Fei, *Angew. Chem. Int. Ed.* **2021** , 60 , 17388.
- [20] Z. Cao, S. B. Zacate, X. Sun, J. Liu, E. M. Hale, W. P. Carson, S. B. Tyndall, J. Xu, X. Liu, X. Liu, C. Song, J.-h. Luo, M.-J. Cheng, X. Wen, W. Liu, *Angew. Chem. Int. Ed.* **2018** , 57 , 12675.
- [21] H. Li, P. Wen, D. S. Itanze, Z. D. Hood, X. Ma, M. Kim, S. Adhikari, C. Lu, C. Dun, M. Chi, Y. Qiu, S. M. Geyer, *Nat. Commun.* **2019** , 10, 5724.
- [22] Y. -N. Gong, L. Jiao, Y. Qian, C. -Y. Pan, L. Zheng, X. Cai, B. Liu, S. -H. Yu, H.-L. Jiang, *Angew. Chem.* **2020** , 132, 2727–2731.
- [23] J. Di, C. Chen, S. -Z. Yang, S. Chen, M. Duan, J. Xiong, C. Zhu, R. Long, W. Hao, Z. Chi, H. Chen, Y. -X. Weng, J. Xia, L. Song, S. Li, H. Li, Z. Liu, *Nat. Commun.* **2019** , 10, 2840.
- [24] T. Zheng, K. Jiang, N. Ta, Y. Hu, J. Zeng, J. Liu, H. Wang, *Joule* , **2019** , 3, 1, 265-278.
- [25] D. Li, M. Kassymova, X. Cai, S. -Q. Zang, H.-L. Jiang, *Coord. Chem. Rev.* **2020** , 421, 1, 213262.
- [26] A. Xu, S. -F. Hugn, A. Cao, Z. Wang, N. Karmodak, J. E. Huang, Y. Yan, A. S. Rasouli, A. Ozden, F. -Y. Wu, Z. -Y. Lin, H. -J. Tsai, T. -J. Lee, F. Li, M. Luo, Y. Wang, X. Wang, J. Abed, Z. Wang, D. -H. Nam, Y. C. Li, A. H. Ip, D. Sinton, C. Dong, E. H. Sargent, *Nat. Catal.* **2022** , 5, 1081-1088.
- [27] N. -Y. Huang, X. -W. Zhang, Y. -Z. Xu, P. -Q. Liao, X. -M. Chen, *Chem. Commun.* **2019** , 55, 14781-14784.
- [28] S. Nitopi, E. Bertheussen, S. B. Scott, X. Liu, A. K. Engstfeld, S. Horch, B. Seger, I. E. L. Stephens, K. Chan, C. Hahn, J. K. Nørskov, T. F. Jaramillo, I. Chorkendorff, *Chem. Rev.* **2019** , 119, 12, 7610–7672.

- [29] D. Cheng, Z. -J. Zhao, G. Zhang, P. Yang, L. Li, H. Gao, S. Liu, X. Chang, S. Chen, T. Wang, G. A. Ozin, Z. Liu, J. Gong, *Nat. Commun.* **2021**, 12, 395.
- [30] C. Choi, S. Kwon, T. Cheng, M. Xu, P. Tieu, C. Lee, J. Cai, H. M. Lee, X. Pan, X. Duan, W. A. Goddard III, Y. Huang, *Nat. Catal.***2020** , 3 804-812.
- [31] Y. Wang, J. Liu, Y. Wang, Y. Wang, G. Zheng, *Nat. Commun.* **2018** , 9, 5003.
- [32] B. Liu, T. Wang, S. Wang, G. Zhang, D. Zhong, T. Yuan, H. Dong, B. Wu, J. Gong, *Nat. Commun.* **2022** , 13, 7111.
- [33] M. Schreier, L. Curvat, f. Giordano, L. Steier, A. Abate, S. M. Zakeeruddin, J. Luo, M. T. Mayer, M. Gratzel, *Nat. Commun.***2015** , 6, 7326.
- [34] C. Liu, B. E. Colon, P. A. Silver, D. G. Nocera, *J. Photochem. Photobiol. A: Chem.* **2018** , 358, 411-415.
- [35] J. Kim, Y. W. Lee, E. G. Choi, P. Boonmongkolras, B. W. Jeon, H. Lee, S. T. Kim, S. K. Kuk, Y. H. Kim, B. Shin, C. B. Park, *J. Mater. Chem. A* , **2020** , 8, 8496-8502.
- [36] D. Scarpa, M. Sarno, *Catalysts* **2022** , 12 (3), 275.
- [37] X. -L. Lu, X. Rong, C. Zhang, T.-B. Lu, *J. Mater. Chem. A* . **2020** , 8, 10695-10708.
- [38] H. Xie, T. Wang, J. Liang, Q. Li, S. Sun, *Nano today***2018** , 21, 41-54.
- [39] W. Zhu, R. Michalsky, Ö. Metin, H. LV, S. Guo, C. J. Wright, X. Sun, A. A. Peterson, S. Sun, *J. Am. Chem. Soc.* **2013** , 135, 45, 16833–16836.
- [40] J. Wang, G. Wang, J. Zhang, Y. Wang, H. Wu, X. Zheng, J. Ding, X. Han, Y. Deng, W. Hu, *Angew. Chem. Int. Ed.* **2021** , 60, 7602–7606.
- [41] J. Zeng, W. Zhang, Y. Yang, D. Li, X. Yu, Q. Gao, *ACS Appl. Mater. Interfaces* **2019** , 11, 36, 33074–33081.
- [42] M. Jia, Q. Fan, S. Liu, J. Qiu, Z. Sun, *Curr. Opin. Green Sustain. Chem.* **2019** , 16, 1–6.
- [43] Q. Hu, J. H. Lee, D. Liu, Y. Liu, Z. Lin, Z. Xie, S. Hwang, S. Kattel, L. Song, J. G. Chen, *Adv. Funct. Mater.* **2020** , 30, 20004.
- [44] J. Gu, C. -S. Hsu, L. Bai, H. M. Chen, X. Hu, *Science***2019** , 364, 1091–1094.
- [45] Y. -C. Hsieh, S. D. Senanayake, Y. Zhang, W. Xu, D. E. Polyansky, *ACS Catal.* **2015** , 5, 9, 5349–5356.
- [46] C. Luan, Y. S hao, Q. Lu, S. Gao, K. Huang, H. Wu, K. Yao, *ACS Appl. Mater. Interfaces* **2018** , 10, 21, 17950–17956.
- [47] W. Zhu, Y. -J. Zhang, H. Zhang, H. Lv, Q. Li, R. Michalsky, A. A. Peterson, S. Sun, *J. Am. Chem. Soc.* **2014** , 136, 46, 16132–16135.
- [48] M. N. Hossain, Z. Liu, J. Wen, A. Chen, *Appl. Catal. B* . **2018** , 236, 483–489.
- [49] S. Zhu, Q. Wang, X. Qin, M. Gu, R. Tao, B. P. Lee, L. Zhang, Y. Yao, T. Li, M. Shao, *Adv. Energy Mater.* **2018** , 8, 180223.
- [50] W. Luo, J. Zhang, M. Li, A. Züttel, *ACS Catal.* **2019** , 9, 5, 3783–3791.
- [51] M. Wang, Q. Xie, H. Chen, G. Liu, X. Cui, L. Jiang, *Chinese J. Catal.* **2021** , 42, 2306–2312.
- [52] L. -W. Xu, S. -L. Qian, B. -X. Dong, L. -G. Feng, Z. -W. Li, *J. Mater. Sci.* **2022**, 57, 526–537. [53] Z. Song, L. Zhang, K. D. Davis, X. Fu, J. -L. Luo, X. Sun, *Adv. Energy Mater.* **2020** , 10, 2001561.
- [54] S. Shoaib, A. Shah, T. Najam, M. Wen, S.-Quan. Zang, A. Waseem, H.-L. Jiang, *Small Struct.* **2022** , 3, 210.

- [55] Y. Wang, P. Hou, Z. Wang, P. Kang, *ChemPhysChem* **2017** , 18, 3142–3147.
- [56] L. Zhou, H. Li, D. Wang, W. Jiang, Y. Wu, L. Shang, C. Guo, C. Liu, B. Ren, *Electroanalysis* **2022** , 34, 1–12.
- [57] T. Zhang, Y. Qiu, P. Yao, X. Li, H. Zhang, *ACS Sustainable Chem. Eng.* **2019** , 7, 18, 15190–15196.
- [58] S. Kim, W. J. Dong, S. Gim, W. Sohn, J. Y. Park, C. J. Yoo, H. W. Jang, J. -L. Lee, *Nano Energy* **2017** , 39, 44–52.
- [59] Q. Wei, J. Qin, G. Jia, Y. Zhao, Z. Guo, G. Cheng, W. Ma, W. Yang, Z. Zhang, *J. Phys. Chem. Lett.* **2022** , 13, 39, 9058–9065.
- [60] S. Ma, M. Sadakiyo, M. Heima, R. Luo, R. T. Haasch, J. I. Gold, M. Yamauchi, P. J. A. Kenis, *J. Am. Chem. Soc.* **2017**, 139, 1, 47–50.
- [61] S. Nitopi, E. Bertheussen, S. B. Scott, X. Liu, A. K. Engstfeld, S. Horch, B. Seger, I. E. L. Stephens, K. Chang, C. Hahn, J. K. Norskov, T. F. Jaramillo, I. Chorkendorff. *Chem. Rev.* **2019** , 119, 12, 7610–7672.
- [62] G. L. D. Gregorio, T. Burdyny, A. Loiudice, P. Lyengar, W. A. Smith, R. Buonsanti, *ACS Catal.* **2020** , 10, 9, 4854–4862.
- [63] B. Zhang, J. Zhang, M. Hua, Q. Wan, Z. Su, X. Tan, L. Liu, F. Zhang, G. Chen, D. Tan, X. Cheng, B. Han, L. Zheng, G. Mo, *J. Am. Chem. Soc.* **2020**, 142, 31, 13606–13613.
- [64] W. Liu, P. Zhai, A. Li, B. Wei, K. Si, Y. Wei, X. Wang, G. Zhu, Q. Chen, X. Gu, R. Zhang, W. Zhou, Y. Gong, *Nat. Commun.* **2022**, 13, 1877.
- [65] Y. Li, F. Cui, M. B. Ross, D. Kim, Y. Sun, P. Yang, *Nano Lett.* **2017** , 17, 2, 1312–1317.
- [66] J. Zhang, W. Cai, F. X. Hu, H. Yang, B. Liu, *Chem. Sci.* **2021** , 12, 6800–6819.
- [67] X. -F. Yang, A. Wang, B. Qiao, J. Li, J. Liu, T. Zhang, *Acc. Chem. Res.* **2013** , 46, 8, 1740–1748.
- [68] H. Zhang, G. Liu, L. Shi, J. Ye, *Adv. Energy Mater.* **2018** , 8, 17013.
- [69] H. Xu, Y. Zhao, Q. Wang, G. He, H. Chen, *Coord. Chem. Rev.* **2022** , 451, 214261.
- [70] X. Li, W. Bi, M. Chen, Y. Sun, H. Ju, W. Yan, J. Zhu, X. Wu, W. Chu, C. Wu, Y. Xie, *J. Am. Chem. Soc.* **2017** , 139, 42, 14889–14892.
- [71] C. Yan, H. Li, Y. Ye, H. Wu, F. Cai, R. Si, J. Xiao, S. Miao, S. Xie, F. Yang, Y. Li, G. Wang, X. Bao, *Energy Environ. Sci.* **2018** , 11, 1204–1210.
- [72] Y. Pan, R. Lin, Y. Chen, S. Liu, W. Zhu, X. Cao, W. Chen, K. Wu, W. -C. Cheong, Yu Wang, L. Zheng, J. Luo, Y. Lin, Y. Liu, C. Liu, J. Li, Q. Lu, X. Chen, D. Wang, Q. Peng, C. Chen, Y. Li, *J. Am. Chem. Soc.* **2018** , 140, 12, 4218–4221.
- [73] L. Han, S. Song, M. Liu, S. Yao, Z. Lian, H. Cheng, Z. Ren, W. Liu, R. Lin, G. Qi, X. Liu, Q. Wu, J. Luo, H. L. Xin, *J. Am. Chem. Soc.* **2020** , 142, 29, 12563–12567.
- [74] S. Wu, X. Lv, D. Ping, G. Zhang, S. Wang, H. Wang, X. Yang, D. Guo, S. Fang, *Electrochim. Acta* **2020** , 340, 135930.
- [75] J. Guo, W. Zhang, L. H. Zhang, D. Chen, J. Zhan, X. Wang, N. R. Shiju, F. Yu, *Adv. Sci.* **2021** , 8, 210288.
- [76] S. Chen, X. Li, C. W. Kao, T. Luo, K. Chen, J. Fu, C. Ma, H. Li, M. Li, T. S. Chan, M. Liu, *Angew. Chem. Int. Ed.* **2022**, 61, e2022.
- [77] M. Wang, W. Yang X. Li, Y. Xu, L. Zheng, C. Su, B. Liu, *ACS Energy Lett.* **2021** , 6, 2, 379–386.

- [78] X. Ma, J. Du, H. Sun, F. Ye, X. Wang, P. Xu, C. Hu, L. Zhang, D. Liu, *Appl. Catal. B.* **2021** , 298, 120543.
- [79] X. Liang, N. Tian, Z. Zhou, S. Sun, *ACS Sustainable Chem. Eng.* **2022** , 10, 5, 1880–1887.
- [80] H. Cui, Y. Guo, L. Guo, L. Wang, Z. Zhou, Z. Peng, *J. Mater. Chem. A* **2018** , 6, 18782-18793.
- [81] S. Liu, M. Jin, J. Sun, Y. Qin, S. Gao, Y. Chen, S. Zhang, J. Luo, X. Liu, *Chem. Eng. J.* **2022** , 437, 135294.
- [82] P. Chen, Y. Zhang, Y. Zhou, F. Dong, *Nano Materials Science* **2021** , 3, 344–36.
- [83] P. Ding, T. Jiang, N. Hang, Y. Li, *Mater. Today Nano***2020** , 10, 1000773.
- [84] Y. Chen, Y. Liu, F. Wang, X. Guan, L. Guo, *Journal of Energy Chemistry* **2021** , 61, 469-488.
- [85] Y. Li, T. Wang, B. Gao, X. Fan, H. Gong, H. Xue, S. Zhang, X. Huang, J. He, J. Zheng, Y. Lyu, B. Wu, S. *New J. Chem.***2021** , 45, 3463-3468
- [86] J. Zheng, Y. Lyu, B. Wu, S. Wang, *EnergyChem***2020** , 2, 100039.
- [87] J. Oh, T. G. Deutsch, H. C. Yuan, H. M. Branz, *Energy Environ. Sci.* **2011** , 4, 1690-1694.
- [88] D. J. Lee, G. M. Kumar, V. Ganesh, H. C. Jeon, D.Y. Kim, T. W. Kang, P. Ilanchezhian, *Nanomaterials* **2022** , 12 (18), 3192.
- [89] L. He, D. Lai, H. Wang, C. Jian, Rusli, *Small***2012** , 8, 11, 1664-1668.
- [90] J. T. Song, H. Ryoo, M. Cho, J. Kim, J. G. Kim, S. Y. Chung, J. Oh, *Adv. Energy Mater.* **2017** , 7, 16011.
- [91] Y. J. Jang, J. W. Jang, J. Lee, J. H. Kim, H. Kumagai, J. Lee, T. Minegishi, J. Kubota, K. Domen, J. S. Lee, *Energy Environ. Sci.* **2016** , 9, 1114-1114.
- [92] K. Wang, N. Fan, B. Xu, Z. Wei, C. Chen, H. Xie, W. Ye, Y. Peng, M. Shen, R. Fan, *Small* **2022** , 18, 22012.
- [93] Y. Hu, F. Chen, P. Ding, H. Yang, J. Chen, C. Zha, Y. Li, *J. Mater. Chem. A* . **2018** , 6, 21906-21912.
- [94] S. K. Choi, U. Kang, S. Lee, D. J. Ham, S. M. Ji, H. Park, *Adv. Energy Mater.* . **2014** , 4, 13014.
- [95] P. Ding, Y. Hu, J. Deng, J. Chen, C. Zha, H. Yang, N. Han, Q. Gong, L. Li, T. Wang, X. Zhao, Y. Li, *Mater. Today Chem.* **2019** , 11, 80e85.
- [96] W. Ma, M. Xie, S. Xie, L. Wei, Y. Cai, Q. Zhang, Y. Wang, *Journal of Energy Chemistry* **2021** , 54, 422–428.
- [97] X. Deng, R. Li, S. Wu, L. Wang, J. Hu, J. Ma, W. Jiang, N. Zhang, X. Zheng, C. Gao, L. Wang, Q. Zhang, J. Zhu, Y. Xiong, *J. Am. Chem. Soc.* **2019** , 141, 27, 10924–10929.
- [98] Q. Shen, Z. Chen, X. Huang, M. Liu, G. Zhao, *Environ. Sci. Technol.* **2015** , 49, 9, 5828–5835.
- [99] Y. Shi, T. –Y. Hsieh, M. A. Hoque, W. Cambarau, S. Narbey, C. G. –Surinach, E. Palomares, M. Lanza, A. Llobet, *ACS Appl. Mater. Interfaces* **2020** , 12, 50, 55856–55864.
- [100] N. C. D. Nath, S. Y. Choi, H. W. Jeong, J. –J. Lee, H. Park, *Nano Energy* **2016** , 25, 51-59.
- [101] W. Deng, L. Zhang, H. Dong, X. Chang, T. Wang, J. Gong, *Chem. Sci.* **2018**, 9, 6599-6604.
- [102] C. Chen, X. Sun, D. Yang, L. Lu, H. Wu, L. Zheng, P. An, J. Zhang, B. Han, *Chem. Sci.* **2019** , 10, 1659-1663.
- [103] R. Daiyan, X. Lu, Y. H. Ng, R. Amal, *Catal. Sci. Technol.* **2017** , 7 , 2542-2550.

- [104] Y. Wang, J. Liu, Y. Wang, Y. Wang, G. Zheng, *Nat. Commun.* **2018**, 9, 5003.
- [105] W. H. Lee, C. Lim, E. Ban, S. Bae, J. Ko, H. -S. Lee, B. K. Min, K. -Y. Lee, J. S. Yu, H. -S. Oh, *Appl. Catal. B: Environ.***2021**, 297, 120427.
- [106] B. Kim, H. Seong, J. T. Song, K. Kwak, H. Song, Y. C. Tan, G. Park, D. Lee, J. Oh, *ACS Energy Lett.* **2020**, 5, 3, 749–757.
- [107] X. Chen, H. Chen, W. Zhou, Q. Zhang, Z. Yang, Z. Li, F. Yang, D. Wang, J. Ye, L. Liu, *Small* **2021**, 17, 2101128.
- [108] D. Ren, N. W. X. Loo, L. Gong, B. S. Yeo, *ACS Sustainable Chem. Eng.* **2017**, 5, 10, 9191–9199.
- [109] M. Jilakian, T. H. Ghaddar, *ACS Appl. Energy Mater.* **2022**, 5, 1, 257–265.
- [110] J. Kim, S. Jeong, M. Baek, J. Park, K. Kwon, *Chem. Eng. J.* **2022**, 428, 15, 130259.
- [111] T. N. Huan, D. A. D. Corte, S. Lamaison, D. Karapinar, L. Lutz, N. Menguy, M. Foldyna, S. -H. T. -Cruz, A. Hagfeldt, F. Bella, M. Fontecave, V. Mougél, *Proc. Natl. Acad. Sci. U.S.A.***2019**, 116(20), 9735-9740.
- [112] Gurudayal, J. Ager, N. Mathews, in *Halide Perovskites*,**2018**, 273– 292.
- [113] Y. Hori, I. Takahashi, O. Koga, N. Hoshi, *J. Mol. Catal. A: Chem.* **2003**, 199, 39–47.
- [114] Y. Huang, C. W. Ong, B. S. Yeo, *ChemSusChem* **2018**, 11, 3299.
- [115] C. Hahn, T. Hatsukade, Y. -G. Kim, A. Vailionis, J. H. Baricuatro, D. C. Higgins, S. A. Nitopi, M. P. Soriaga, T. F. Jaramillo, *Proc. Natl. Acad. Sci. U.S.A.* **2017**, 114(23), 5918-5923.
- [116] R. Reske, H. Mistry, F. Behafarid, B. R. Cuenya, P. Strasser, *J. Am. Chem. Soc.* **2014**, 136, 19, 6978–6986.
- [117] K. Yao, Y. Xia, J. Li, N. Wang, J. Han, C. Gao, M. Han, G. Shen, Y. Liu, A. Seifitokaldani, X. Sun, H. Liang, *J. Mater. Chem. A*, **2020**, 8, 11117-11123.
- [118] D. Gao, Y. Zhang, Z. Zhou, F. Cai, X. Zhao, W. Huang, Y. Li, J. Zhu, P. Liu, F. Yang, G. Wang, X. Bao, *J. Am. Chem. Soc.* **2017**, 139, 16, 5652–5655.
- [119] P. -P. Yang, X. -L. Zhang, F. -Y. Gao, Y. -R. Zheng, Z. -Z. Niu, X. Yu, R. Liu, Z. -Z. Wu, S. Qin, L. -P. Chi, Y. Duan, T. Ma, X. -S. Zheng, J. -F. Zhu, H. -J. Wang, M. -R. Gao, S. -H. Yu, *J. Am. Chem. Soc.* **2020**, 142, 13, 6400–6408.
- [120] X. Feng, K. Jiang, S. Fan, M. W. Kanan, *ACS Cent. Sci.* **2016**, 2, 3, 169–174.
- [121] Z. Chen, T. Wang, B. Liu, D. Cheng, C. Hu, G. Zhang, W. Zhu, H. Wang, Z. -J. Zhao, J. Gong, *J. Am. Chem. Soc.* **2020**, 142, 15, 6878–6883.
- [122] T. N. Huan, D. A. D. Corte, S. Lamaison, D. Karapinar, L. Lutz, N. Menguy, M. Foldyna, S. -H. T. -Cruz, A. Hagfeldt, F. Bella, M. Fontecave, V. Mougél, *Proc. Natl. Acad. Sci. U.S.A.***2019**, 116(20), 9735-9740.
- [123] G. Zhang, Z. -J. Zhao, D. Cheng, H. Li, J. Yu, Q. Wang, H. Gao, J. Guo, H. Wang, G. A. Ozin, T. Wang, J. Gong, *Nat. Commun.* **2021**, 12, 5745.
- [124] W. -H. Cheng, M. H. Richter, R. Muller, M. Kelzenberg, S. Yalamanchili, P. R. Jahelka, A. N. Perry, P. C. Wu, R. Saive, F. Dimroth, B. S. Brunschwig, T. Hannappel, H. A. Atwater, *Adv. Energy Mater.* **2022**, 12, 2201062.
- [125] Y. Sugano, A. Ono, R. Kitagawa, J. Tamura, M. Yamagiwa, Y. Kuddo, E. Tsutsumi, S. Mikoshiba, *RSC Adv.***2015**, 5, 54246-54252.

- [126] Y. J. Jang, I. Jeong, J. Lee, J. Lee, M. J. Ko, J. S. Lee, *ACS Nano* **2016** , 10, 6980-6987.
- [127] J. Kim, Y. W. Lee, E. -G. Choi, P. Boonmongkolras, B. W. Jeon, H. Lee, S. T. Kim, S. K. Kuk, Y. H. Kim, B. Shin, C. B. Park, *J. Mater. Chem. A* , **2020** , 8, 8496-8502.
- [128] Gurudayal, J. W. Beeman, J. Bullock, H. Wang, J. Eichhorn, C. Towle, A. Javey, F. M. Toma, N. Mathews, J. W. Ager, *Energy Environ. Sci.* **2019** , 12, 1068—1077.

TABLE 1 Summary of electrocatalysts for CO₂RR.

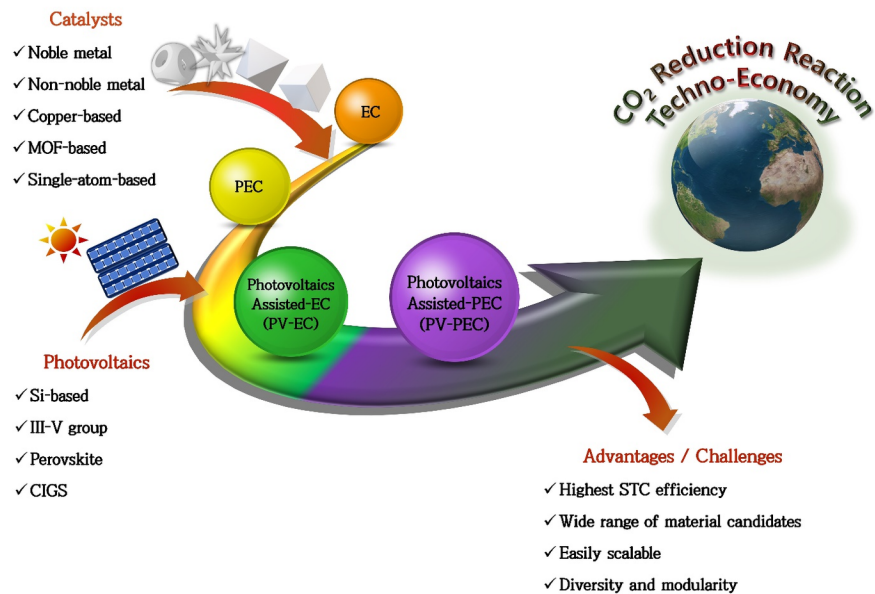
Materials	Electrolyte	Product	FE (%)	Ref
Ag nanocorals	0.1M KHCO ₃	CO	95	45
Ag-200nm NWA	0.5M KHCO ₃	CO	91	46
Ag NWs	0.5M KHCO ₃	CO	94	47
NP Au	0.1M NaHCO ₃	CO	95.86	48
Pd-Au NWs	0.5M KHCO ₃	CO	94.3	49
P-Zn	0.1M KHCO ₃	CO	95	50
N,O-Ni/CMK3	0.5M KHCO ₃	CO	97	51
PCN-222(Fe)	0.5M KHCO ₃	CO	95.5	52
ZIF-8 ^{SO} ₄	0.5M NaCl	CO	65.5	55
ZIF-8 _{80nm}	0.5M KHCO ₃	CO	90	56
Bi-modified Zn	0.5M NaHCO ₃	HCOO ⁻	94	57
Bi nanoflakes	0.1M KHCO ₃	HCOO ⁻	100	58
Np-Bi	0.5M KHCO ₃	HCOO ⁻	94	59
n-CuNS	0.1M KHCO ₃	C ₂ H ₄	83.2	63
R-CuO-NPs	0.5M KCl	C ₂ H ₄	84.5	64
Cu NW	0.1 M KHCO ₃	CH ₄	55	65
Ni-N ₄ -C	0.5M KHCO ₃	CO	99	70
C-Zn ₁ Ni ₄ ZIF-8	0.1M KHCO ₃	CO	98	71
SPCo-N ₅ /HNPCSs	0.2 NaHCO ₃	CO	99.4	72
SA-Zn/MNC	1M KHCO ₃	CO	85	73
Fe-N-C-0.5	0.5M KHCO ₃	CO	95	74
Sn-NOC	0.1M KHCO ₃	CO	94	75
Fe-SA/BNC	0.1 M KHCO ₃	CO	94	81

TABLE 2 Summary of co-catalysts for PEC CO₂reduction

Photocathode	Co-catalyst	Electrolyte	Product	FE (%)	Ref
pn ⁺ -Si	RA-Au film	0.2M KHCO ₃	CO	91	90
ZnTe/ZnO-nanowire	Au NPs	0.5M KHCO ₃	CO	97	91
TiO ₂ /n+p- Si	Au NPs	0.1M KHCO ₃	CO	86	92
p-Si photocathode	Particulate Ag film	0.5M KHCO ₃	CO	90	93
p-Si nanowire	Sn NPs	0.1M KHCO ₃	HCOO ⁻	88	94
p-Si photocathode	Bi film	0.5M KHCO ₃	HCOO ⁻	90	95
p-0Si nanowire arrays	Ni@In core-shell	0.1M KHCO ₃	HCOO ⁻	8	96
Cu ₂ O photocathode	Cu ₃ (BTC) ₂	4M NaOH	CO	95	97
Co ₃ O ₄ NTs arrays	Cu NPs	0.1M Na ₂ SO ₄	HCOO ⁻	production rate of 6.75 mmol·L ⁻¹ ·cm ⁻²	98

TABLE 3 Summary of PV-EC and PV-PEC devices for CO₂RR

PV-assisted CO ₂ RR device	CO ₂ RR catalyst	OER catalyst	Photovoltaics	Product	FE (%)	Solar-to-Energy (%)	Ref.
PV-EC	Disordered Ag	Pt-foil	Si	CO	92.8%	~0.1% (Solar-to-CO)	101
PV-EC	Needle-like Nano-Au	Nanosheet-like NiFe hydroxide	GaAs (InGaP/GaAs/Ge)	CO	92%	15.6% (Solar-to-CO)	104
PV-EC	W@AgD	Fe-doped Co foam	Si	CO	95%	12.1% (Solar-to-CO)	105
PV-EC	Au ₂₅ cluster	NiFe inverse opal	Ga _{0.5} In _{0.5} P/GaAs	CO	90%	18% (Solar-to-CO)	106
PV-EC	Boron-doped bismuth (Bi(B))	FeP nanosheet	GaInP/GaInAs/GaIn	Formate	93%	11.8% (Solar-to-formate)	107
PV-EC	Oxide-derived Cu	In ₂ O ₃	Si	C ₂ H ₄	31.9%	2.9% (Solar-to-fuel)	108
PV-EC	Grain-boundary-rich Cu	Se-(NiCo)S _x /(OH) nanosheets	a-Si/c-Si heterojunction	C ₂ H ₅ OH	31.74%	3.8% (Solar-to-C ₂ +))	121
PV-EC	Dendritic nanostructured CuO (DN-CuO)	Dendritic nanostructured CuO (DN-CuO)	Perovskite	C ₂ H ₄	34%	2.3% (Solar-to-hydrocarbon)	122
PV-EC	High-power reactively sputtered Cu films (HRS-Cu)	Ni foam	Si	C ₂ H ₄	45%	~4% (Solar-to-ethylene)	123
PV-EC	Cu/Ag-PA-FhG-ISE 3J	NiOx	III-V semiconductors	C ₂ H ₅ OH	~15%	5% (Solar-to-fuels)	124
PV-PEC	Pulse-oxidized Au	CoOx	a-Si	CO	>95%	2% (Solar-to-CO)	125
PV-PEC	ZnO@ZnTe@CdTe core-shell nanorod	CdTe-Ci	Perovskite	CO	74.9%	0.43% (Solar-to-fuels)	126
PV-PEC	MesoITO	FeOOH/BiVO ₄	CIGS	Formate	5.6 mM	0.03% (Solar-to-formate)	127
PV-PEC	Ag-supported dendritic Cu	IrO ₂ nanotube	Perovskite	CO	>20%	3.5% (Solar-to-chemical)	128



Scheme 1 Illustration of advances in the CO₂RR systems for techno-economy.

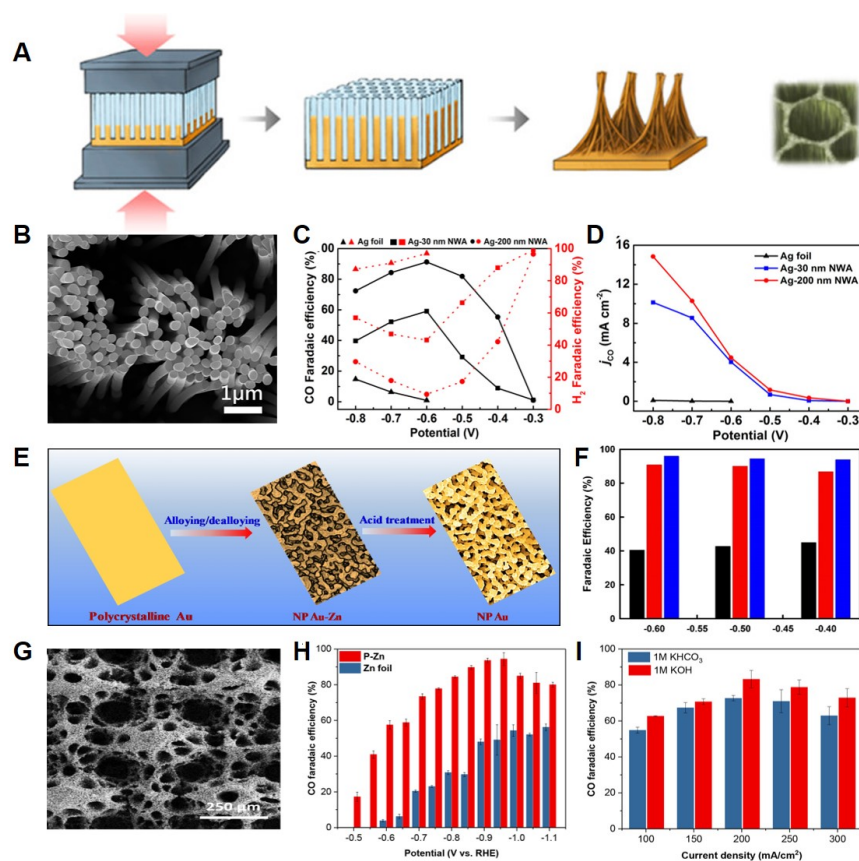


FIGURE 1 Electrochemical performances of noble-based and non-noble based catalysts for CO₂RR. (A)

Schematic of the process of synthesis of Ag NWAs. (B) SEM image of Ag NWA. (C) CO Faradaic efficiencies. (D) Partial CO current density at different applied potentials. Reproduced with the permission.^[46] Copyright 2021, American Chemical Society. (E) Scheme illustration of the fabrication of the NP Au. (F) FE_{CO} of Au, NP Au-Zn, and NP Au. Reproduced with the permission.^[48] Copyright 2018, Elsevier. (G) SEM image of P-Zn electrocatalyst. (H) FE_{CO} of P-Zn in different electrolytes. Reproduced with the permission.^[50] Copyright 2019, American Chemical Society

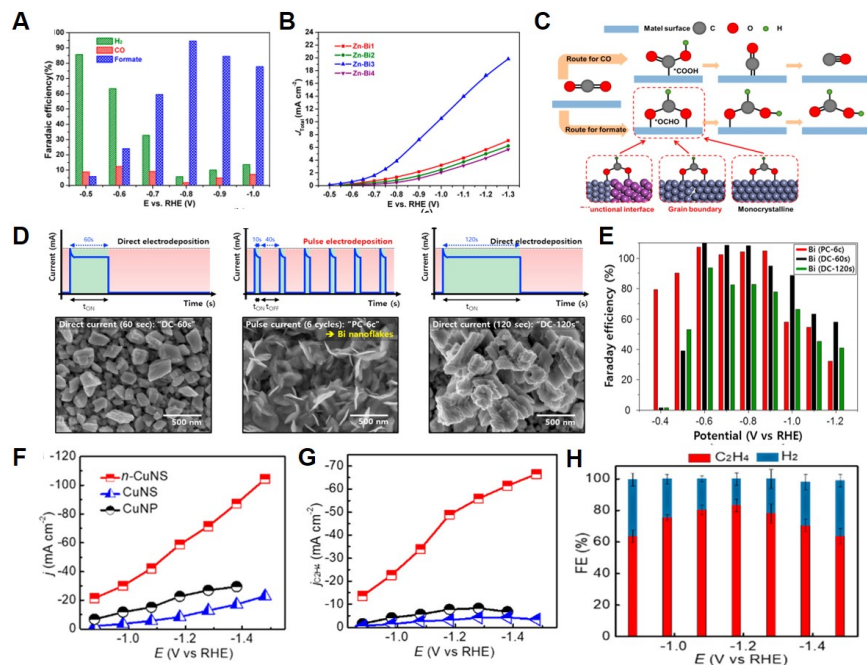


FIGURE 2 Electrochemical performances of non-noble based and Cu based-catalysts for CO_2RR . (A) FE and (B) current density of all different catalysts. (C) CO reduction pathways for CO and formate formation. Reproduced with the permission.^[57] Copyright 2019, American Chemical Society. (D) Schematics of the preparation of the Bi(PC-6c), Bi(DC-60s), and Bi(DC-120s). (E) $HCOO^-$ FE at different potentials. Reproduced with the permission.^[58] Copyright 2017, Elsevier. (F) Total current densities and (G) partial C_2H_4 current densities of n-CuNS, CuNS, and CuNP. (H) FEs of n-CuNS for C_2H_4 and H_2 production. Reproduced with the permission.^[63] Copyright 2020, American Chemical Society

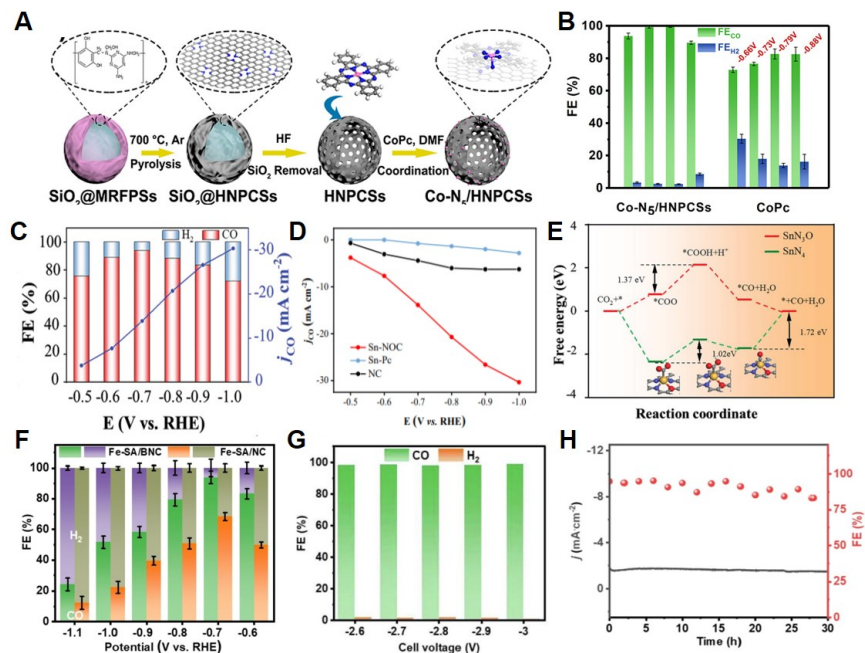


FIGURE 3 Electrochemical performances of SACs for CO₂RR. (A) Schematic of the preparation of Co-N₅/HNPCSS. (B) CO FEs. Reproduced with the permission.^[72] Copyright 2018, American Chemical Society. (C) CO FEs and partial CO current densities of Sn-NOC. (D) CO partial current densities of SN-NOC, Sn-PC, and NC. (E) Free energy diagram for electrochemical CO₂ reduction to CO on Sn₃O and SnN₄. Reproduced with the permission.^[75] Copyright 2021, John Wiley and Sons. (F) FE_{CO} of Fe-SA/BNC using H-cell and (G) using MEA. (H) Electrochemical stability test at -0.7 V vs. RHE. Reproduced with the permission.^[81] Copyright 2022, Elsevier

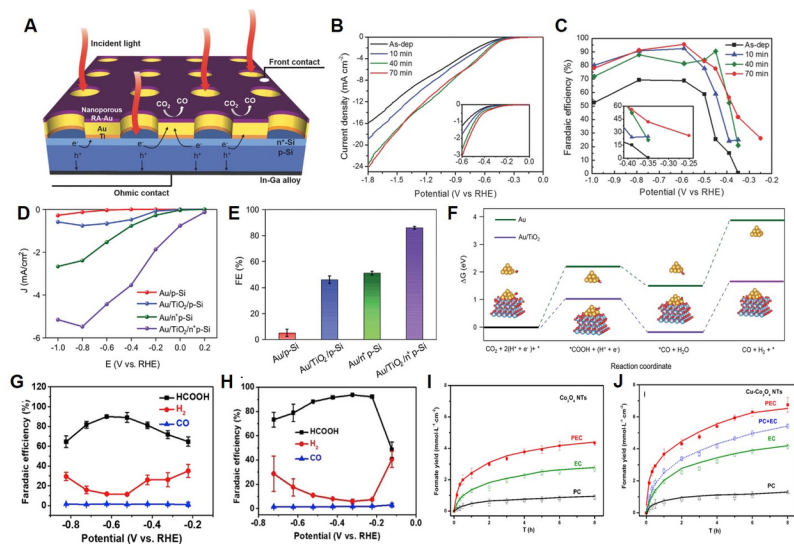


FIGURE 4 Electrochemical performances of co-catalysts for CO₂ reduction. (A) Fabrication process of Nanoporous Au thin films on Si Photoelectrodes. (B) Total current densities of Au thin films. (C) CO FEs at various potentials with different RA treatment times. Reproduced with the permission.^[90] Copyright

2016, John Wiley and Sons. (D) LSV curve and (E) FE_{CO} of Au/p-Si, Au/TiO₂/p-Si, Au/n⁺p-Si, and Au/TiO₂/n⁺p-Si. (F) Free energy diagram of CO₂RR over Au and Au/TiO₂, respectively. Reproduced with the permission.^[92] Copyright 2021, John Wiley and Sons. (G) FEs of formate, H₂, and CO on Si/Bi-15 min. (H) Faradaic efficiencies for formate, H₂, and CO on p-Si/Bi. Reproduced with the permission.^[95] Copyright 2018, Materials Today Chemistry. (I) Formate yield on Co₃O₄ NTs electrode. (J) Formate yield on Cu-Co₃O₄ NTs electrode. Reproduced with the permission.^[98] Copyright 2015, American Chemical Society

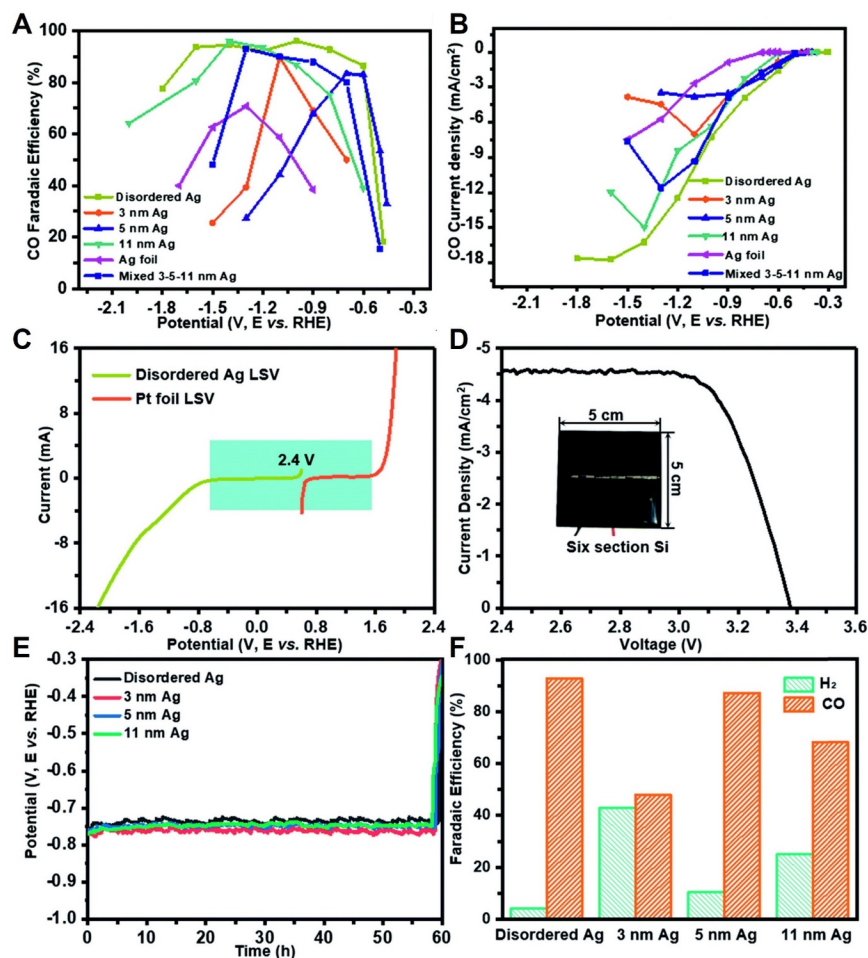


FIGURE 5 PV-EC performance of CO₂RR. (A) FE toward CO in CO₂ saturated 0.1 M KHCO₃ and (B) CO partial current density (j_{CO}) depending over a broad applied potential. (C) The linear sweep voltammetry (LSV) curve of Ag (CO₂RR) and Pt film (HER) at a scan rate of 50 mV s⁻¹. (D) The I/V curve shows the photovoltaic performance of a six-section a-Si cell under AM 1.5 G illumination. (E) Cathode voltage of chronoamperometry measurement (F) and FE toward CO in the PV-EC device characteristic assisted by a six-section a-Si photovoltaics. Reproduced with the permission.^[101] Copyright 2018, Royal Society of Chemistry

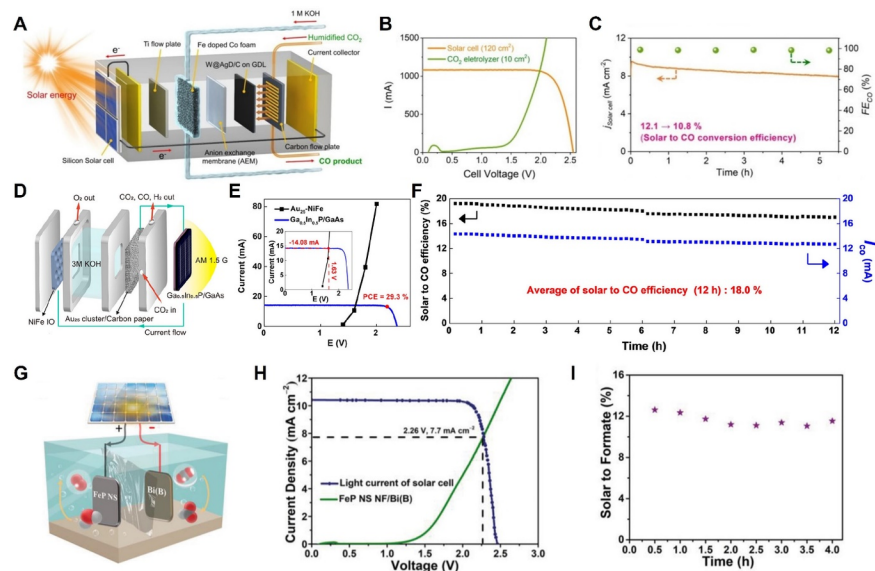


FIGURE 6 PV-EC performance of CO₂RR. (A) Schematic of the PV-EC system. PV-EC device are composed of W@AgD/C on 10 cm² GDL as cathode, 3-6 silicon cells in series as modules with a size of 10 cm x 12 cm, Fe-doped Co foam as anode, and anion exchange membrane. (B) Current density over an applied cell voltage (green) from the *I-V* curve and (C) FE toward CO of photovoltaics-assisted CO₂RR system under AM 1.5 G (orange). Reproduced with the permission.^[105] Copyright 2021, Elsevier. (D) Schematic illustration of the PV-EC device. PV-EC CO₂RR system is composed of Ga_{0.5}In_{0.5}P/GaAs tandem structure as solar cells, Au₂₅ cluster as cathode part, NiFe inverse opal as anode, and 3 M KOH as electrolyte. (E) *I-V* curves of the Ga_{0.5}In_{0.5}P/GaAs tandem photovoltaics and Au₂₅-NiFe under AM 1.5G. (F) STC efficiency of solar-driven CO₂RR during 12 h. Reproduced with the permission.^[106] Copyright 2020, American Chemical Society. (G) Schematic of the PV-EC device. Bi(B) and FeP nanosheets supported on Ni foam were utilized as cathode and anode, respectively, for PV-EC system with GaInP/GaInAs/Ge solar cell. (H) *J-V* curves under AM 1.5 G and (I) STF efficiency during 4 h of PV-CO₂RR system. Reproduced with the permission.^[107] Copyright 2021, John Wiley and Sons

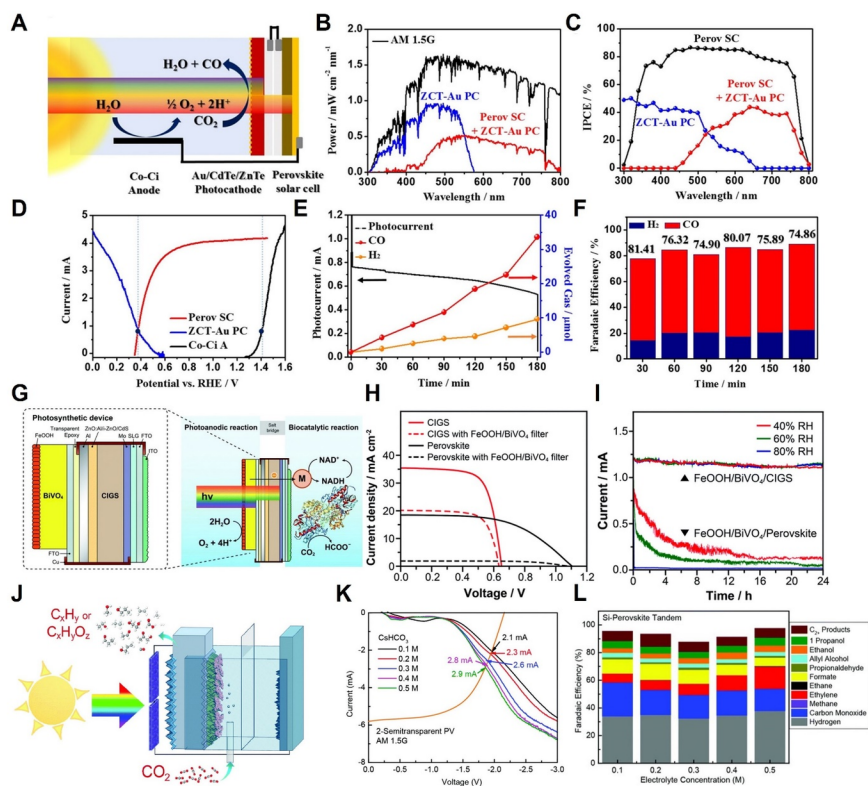


FIGURE 8 PV-PEC performance of CO₂RR. (A) Schematic design of the stacked tandem structure of bias-free PV-PEC system comprising a gold-decorated triple-layer ZnO@ZnTe@CdTe core-shell nanorod array photocathode, CH₃NH₃PbI₃ perovskite solar cell, and Co-Ci anode. (B) Absorption property of two light absorbers under AM 1.5G. (C) Plots of incident photon-to-current conversion efficiency (IPCE) of ZCT-Au-PC, Perov SC and Perov SC + ZCT-Au PC. (D) *J-V* characteristic of PV-PEC in the stacked tandem structure composed of ZCT-Au photocathode and Co-Ci anode. (E) Generated gas production and photocurrent measured by chronoamperometry for 3 h of bias-free PV-PEC device. (F) FEs toward H₂ and CO of the stacked tandem structure of bias-free PV-PEC device measured for 3 h of CO₂RR in CO₂-purged KHCO₃ solution under 1 sun illumination. Reproduced with permission. ^[126] Copyright 2016, American Chemical Society. (G) Schematic diagram of assembled FeOOH/BiVO₄/CIGS tandem device of unbiased PV-PEC system for formate conversion. (H) Comparison of *J-V* profiles of CIGS and perovskite solar absorber with/without FeOOH/Bi/VO₄ filtered light. (I) Chronoamperometry measurement of FeOOH/BiVO₄/CIGS and FeOOH/BiVO₄/Perovskite depending on relative humidity (RH) values. Reproduced with the permission. ^[127] Copyright 2012, Royal Society of Chemistry. (J) Schematic diagram of PV-PEC system comprising an Ag-supported dendritic Cu as Si-photocathode, IrO₂ nanotube anode, with two series-connected semi-transparent halide perovskite solar cells. (K) *J-V* curves of the Si-photocathode (bottom side) and perovskite PV cell (top side) depending on the concentrations of the CsHCO₃ electrolyte under 1 sun illumination. (L) FEs toward value-added carbon compound depending on the concentrations of the CsHCO₃ electrolyte of unbiased Si-perovskite tandem PV-PEC device under 1 sun illumination. Reproduced with the permission. ^[128] Copyright 2019, Royal Society of Chemistry

AUTHOR BIOGRAPHIES



Jin Hyuk Cho is currently pursuing his Ph.D. at the Korea University in the Department of Materials Science and Engineering. His research interests include electrochemical carbon dioxide reduction reactions over metal-organic frameworks and single-atom-based materials.



Joonhee Ma is pursuing her B.S. at Korea University in the Department of Materials Science and Engineering. Her research interests include hydrogen evolution reactions and electrochemical carbon dioxide reduction reactions over metal-organic frameworks and single-atom-based materials.



Soo Young Kim is a professor at the Korea University in the Department of Materials Science and Engineering. He is interested in the modulation of the properties of 2-dimensional materials, halide perovskites, metal-organic frameworks, and multi-component single-atom catalysts, and their applications in various fields such as organic photovoltaics, perovskite solar cells, light emitting diodes, gas sensors, hydrogen evolution reactions, and carbon dioxide reduction reactions.